Marine Pollution Bulletin 137 (2018) 566–581

Contents lists available at ScienceDirect

Marine Pollution Bulletin

journal homepage: www.elsevier.com/locate/marpolbul

Forecasting of oil-spill trajectories by using SCHISM and X-band radar

Chi-Min Chiu[a], Ching-Jer Huang[a,b,*], Li-Chung Wu[b], Yinglong Joseph Zhang[c], Laurence Zsu-Hsin Chuang[a], Yangming Fan[b], Hao-Cheng Yu[d]

[a] Department of Hydraulic and Ocean Engineering, National Cheng Kung University, No. 1, University Road, Tainan City 70101, Taiwan
[b] Coastal Ocean Monitoring Center, National Cheng Kung University, No. 1, University Road, Tainan City 70101, Taiwan
[c] Virginia Institute of Marine Science, College of William & Mary, 1375 Greate Road, Gloucester Point, VA 23062, USA
[d] Department of Marine Environment and Engineering, National Sun Yat-Sen University, 70 Lien-Hai Road, Kaohsiung 80424, Taiwan

ARTICLE INFO

Keywords:
Oil spill
SCHISM
X-band radar
Container ship T. S. Taipei
Oil-spill trajectories

ABSTRACT

In this study, we propose a two-step strategy for tracking oil-spill trajectories. First, an X-band radar is established to monitor oil spills. Accordingly, we propose a radar image-processing technique for identifying the oil slicks from the nautical radar images. Second, we apply the SCHISM to determine the water surface elevations and currents at the event site and obtain the trajectories of the oil slicks using a Lagrangian particle-tracking method incorporated in the SCHISM. An oil-spill event caused by the container ship T. S. Taipei is used as a case study for testing the capability of the proposed oil-tracking strategy. The SCHISM simulation results for the fouled coastline obtained using the wind data from a nearby data buoy agree quite well with those obtained from field observations. However, the predicted fouled coastline based on the forecasted wind data is unsatisfactory. The reasons for the unsatisfactory prediction are discussed and revealed.

1. Introduction

Oil-spill events in coastal areas, harbors, and rivers are usually caused by the grounding of ships, failure of oil rigs, cracked oil pipelines, or damaged oil refineries and storages. Large-volume oil spills in coastal areas often have severe effects on marine ecosystems and economic activities, such as those of the Exxon Valdez oil spill (Peterson et al., 2003) and the Deepwater Horizon oil spill (Crone and Tolstoy, 2010; Kujawinski et al., 2011; French-McCay et al., 2015). The shipping routes in East Asia pass close to Taiwan, and rapid economic development has hastened the development of Taiwan's international shipping industry. In particular, both exports and imports of oil products have increased because of the rapid development of Taiwan's petrochemical industry. However, this has also resulted in an increased risk of oil-spill events in harbor and coastal areas. For example, in January 2001, the Greek merchant vessel Amorgos lost power while en route from India to China and was grounded near Kenting National Park at the southernmost tip of Taiwan Island. Because of the deteriorating weather and sea conditions, the hull of the Amorgos split and approximately 1300 tons of fuel oil leaked from the vessel into the sea surrounding Kenting National Park, causing major damage to the maritime and local environment (https://en.wikipedia.org/wiki/Amorgos_oil_spill). The oil slick fouled more than 3.5 km of the nearby coastline. Recently, in March 2016, a container ship, T. S. Taipei, split into two parts during rough monsoon weather after being grounded one nautical mile off Shimen, close to the northernmost tip of Taiwan Island. According to the Environmental Protection Administration (EPA), Taiwan, the oil slick from the T. S. Taipei fouled more than 9 km of the nearby coastline (EPA Taiwan, 2016; Huang et al., 2016). Accordingly, for the mitigation of oil spills around Taiwan, operational oil-spill response and impact assessment are required.

After oil leaks into the marine environment, it undergoes a continual series of compositional changes that result from a process referred to as “weathering” (Tarr et al., 2016). The weathering processes include spreading, evaporation, entrainment, emulsification, dissolution, biodegradation, photo-oxidation, sedimentation, and stranding (Reed et al., 1999; Fernando, 2012). Spreading and evaporation influence the initial stages of oil spill during the extending phase (Chen et al., 2007). Fay (1969) indicated that oil spills on water tend to spread outward in the form of a thin continuous layer. This tendency to spread is the result of two physical forces: gravity and surface tension. Mackay et al. (1980, 1982) developed a model for simulating oil-spill behavior, such as spreading into thin and thick slicks, drift, evaporation, and the formation of water-in-oil emulsion. For most spills, evaporation is the main mechanism for mass removal from the surface slick. Fingas (1996, 2011) proposed an empirical strategy for modeling evaporation from

* Corresponding author at: Department of Hydraulic and Ocean Engineering, National Cheng Kung University, No. 1, University Road, Tainan City 70101, Taiwan.
E-mail address: cjhuang@mail.ncku.edu.tw (C.-J. Huang).

https://doi.org/10.1016/j.marpolbul.2018.10.060
Received 5 April 2018; Received in revised form 21 October 2018; Accepted 29 October 2018

Fig. 1. SCHISM modeling system (http://ccrm.vims.edu/schismweb/).

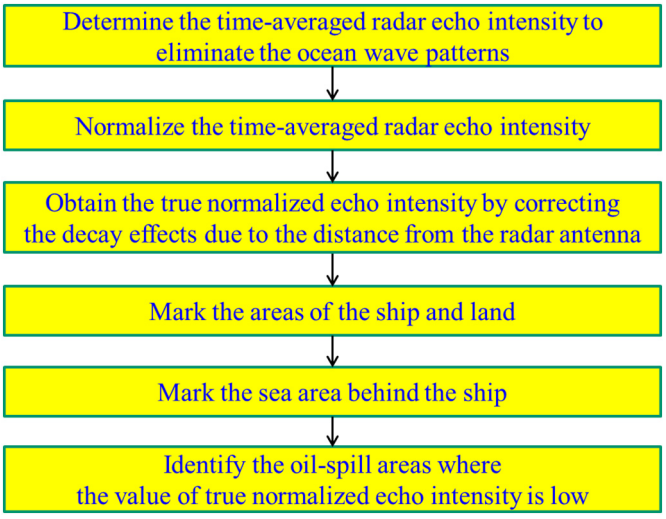

Fig. 2. Proposed radar image-processing technique for identifying oil slicks.

surface spills.

Evaporation transfers oil from the sea surface to the atmosphere, whereas entrainment transports oil from the surface to the water column. Based on laboratory and flume experiments, Delvigne and Sweeney (1988) developed an empirical relation for the oil entrainment rate as a function of the oil type, oil layer thickness, breaking wave energy, and temperature.

Water-in-oil emulsion (or emulsification) is the process in which water is entrained in oil. Emulsification causes significant changes in the volume, density, and viscosity of the slick, and can make the cleanup of oil spills very difficult (NAS, 2003; Fingas, 2014b). Not all oils emulsify; Fingas and Fieldhouse (2003) indicated that crude oil emulsifies when the asphaltene and resin components reach a certain amount of the oil mass. Fingas and Fieldhouse (2011) proposed a stability index (SI) to determine if an oil emulsifies and the type of emulsification. Simecek-Beatty and Lehr (2007) referred to evaporation, dispersion (entrainment), and emulsification as major short-term weathering processes, and they termed the other weathering processes,

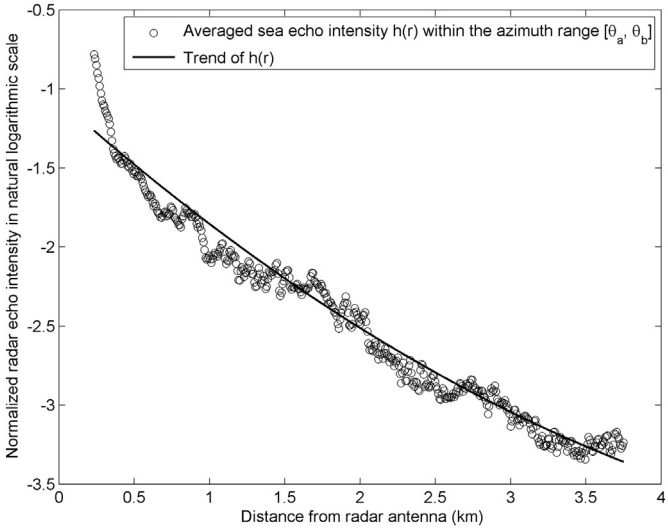

Fig. 3. Decay of radar echo intensities with the distance from the X-band radar.

Fig. 4. Setup of an X-band radar at the coast near the container ship T. S. Taipei for monitoring oil spills.

including dissolution, biodegradation, photo-oxidation, and sedimentation, as minor long-term weathering processes. Oil stranding should also be considered when the oil slick moves toward the shoreline (Diop et al., 2014). A detailed review of oil-spill behavior models can be found in studies such as those of Huang (1983), Reed et al. (1999), French-McCay (2004), Simecek-Beatty and Lehr (2007), and Spaulding (2017).

In addition to the scientific investigations of the oil-spill weathering processes, several oil-spill models have been developed to support operational oil-spill response and impact assessment. These include (i) the oil spill contingency and response model (OSCAR; Reed et al., 2000), (ii) the oil modeling application package (OILMAP; Spaulding et al., 1992), (iii) the spill impact model application package (SIMAP; French-McCay et al., 2015), and (iv) the general National Oceanic and Atmospheric Administration operational modeling environment (GNOME; Zelenke et al., 2012).

Recently, a new model called the semi-implicit cross-scale hydroscience integrated system model (SCHISM) was developed to simulate water surface elevations and currents (Zhang et al., 2016). Yu et al. (2017) applied the SCHISM to simulate multi-scale oceanic processes around Taiwan and demonstrated that the sea surface height and sea surface temperature are similar to those obtained from a reference data-

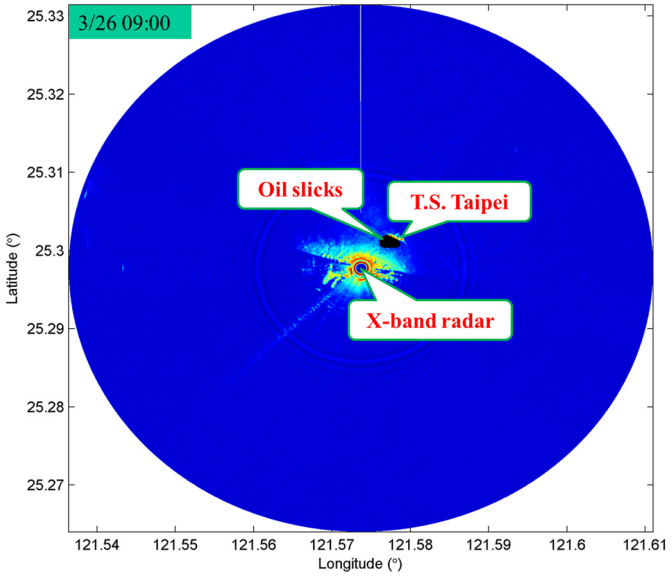

Fig. 5. Identification of the location and extent of oil slicks released from the container ship T. S. Taipei at 09:00 AM on March 26, 2016. Oil slick area is marked black.

assimilated global model. The SCHISM also includes oil-spill modules. Fig. 1 illustrates the complete SCHISM. The oil-spill modules are developed using the Lagrangian particle-tracking methods. The movement of each particle is governed by advection and diffusion processes, and the random walk method is adopted to couple the turbulent diffusion effect.

In most oil drift models, the oil spills are driven by a time series of ocean currents, ocean surface winds, and sea surface temperature to track the oil spills (Cheng et al., 2011). Accordingly, an oil-spill modeling system is usually coupled with hydrodynamic, wind, transport, and oil-weathering models (Beegle-Krause, 2001). The oil-spill model is based on accurately forecasting these dynamic factors (Tkalich, 2006; Guo and Wang, 2009). The oil-spill model can also be used as a fate model to simulate the response actions and estimate the biological effects (Spaulding et al., 1992; Reed et al., 2000; Lehr et al., 2000; French-McCay, 2003, 2004). In addition to the hydrodynamic model, ocean surface currents may be provided using a high-frequency radar (HFR). Offshore data buoys may also provide local meteorological and oceanographic data, such as wind speed and direction, wave height, currents, water temperature, and water level (Herbers et al., 2012; Lin et al., 2017).

Remote-sensing techniques, such as optical and microwave sensors, have also been applied to detect oil spills (Wadsworth et al., 1992; Fingas and Brown, 2014). Remote sensing is superior to in-situ measurements for detecting the spatial patterns of surface slicks. Airborne and satellite-based technologies have been used to detect surface slicks (Klemas, 2010; Leifer et al., 2012). The nautical X-band radar, originally used on ships for navigation safety at sea and near the shore, is currently one of the most prominent remote-sensing tools for monitoring ocean waves and sea surface currents (Young et al., 1985; Alpers and Hühnerfuss, 1988; Nieto Borge and Guedes Soares, 2000; Senet et al., 2001; Gangeskar, 2002; Hessner et al., 2014). Weijenborg (2015) used a land-based X-band radar to continuously measure the ocean surface currents and waves. Although the spatial scale of nautical X-band radar is substantially lower than that of satellite images, it can be easily managed for continuous monitoring of the area of interest. This advantage makes the detection of oil leakage at the primary stage from the ship very efficient.

The key mechanism of radar backscattering from the sea surface is Bragg scattering (Plant, 1990). Waves with wavelength of several centimeters are quite common on the sea surface. These small-scale waves are suitable for the Bragg scattering of X-band electromagnetic waves. When using X-band radar for oil-spill detection, the X-band Bragg waves are suppressed because of the Marangoni effect that causes a resonance-type wave damping in the short-gravity wave region when the sea surface is covered with a viscoelastic film (Alpers and Hühnerfuss, 1988). Consequently, the radar echo intensity is weaker at the region of the oil spill than in the surroundings. Some studies on oil spills have reported that X-band radar yields better results than L- or C–band radars (Fingas and Brown, 1997). The operating distance of the X-band radar for surface slick detection depends on the wind and the

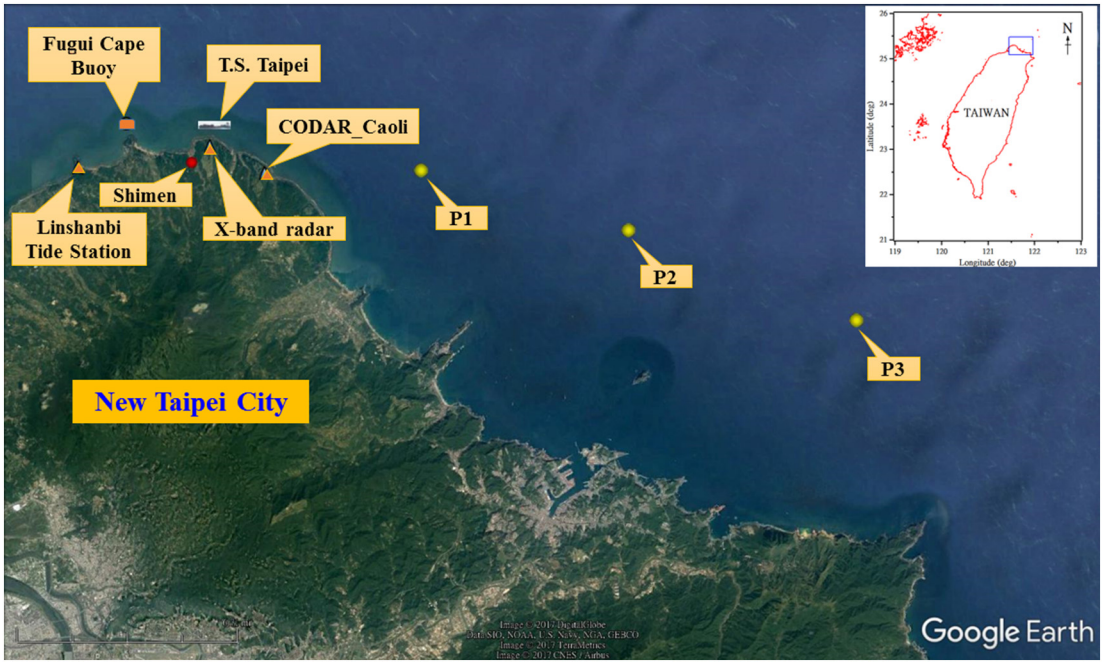

Fig. 6. Map of the Shimen coast (New Taipei City, Taiwan). The time series data of water elevation obtained from the Linshanbi tide station, and the current speeds at P1, P2, and P3 obtained from the Caoli HFR station were selected for comparing with the simulation results obtained from the SCHISM.

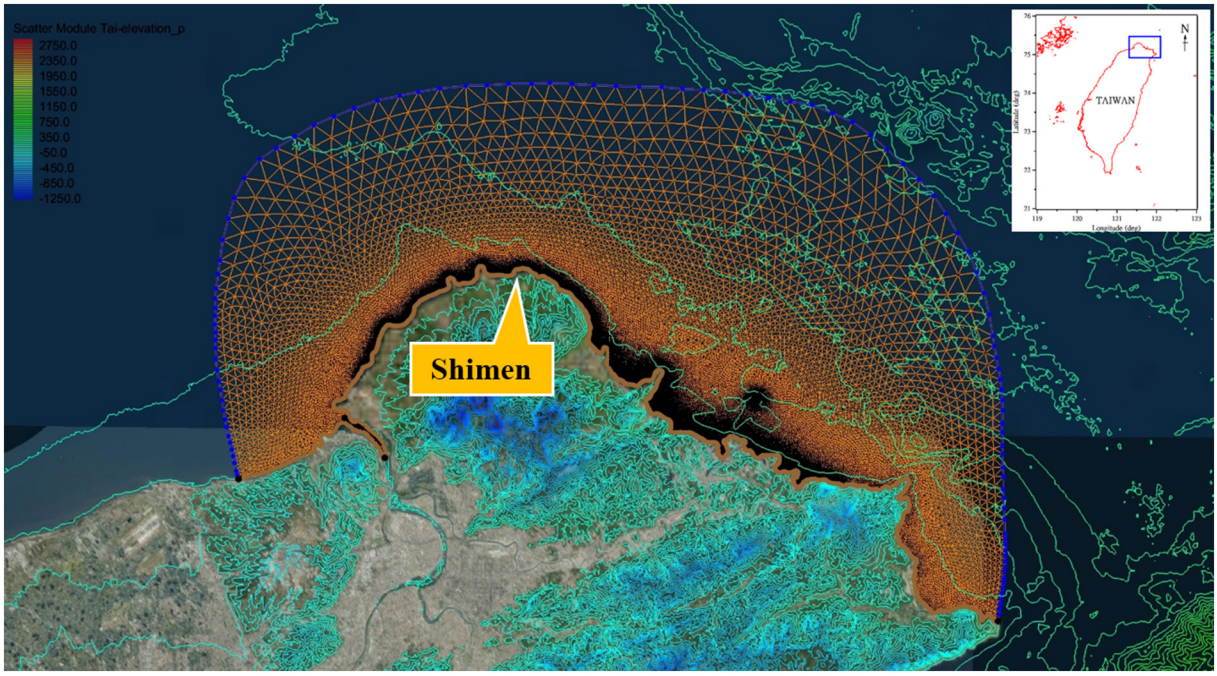

Fig. 7. Computational domain and unstructured triangular mesh near the Shimen coast.

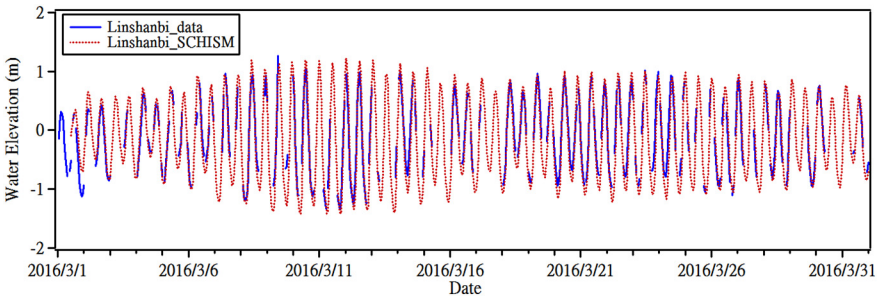

Fig. 8. Comparison of the observed (blue line) and simulated (red dots) time series data of water elevation at Linshanbi tidal station from March 1 to 31, 2016. (For interpretation of the references to color in this figure legend, the reader is referred to the web version of this article.)

grazing angle of the radar antenna. Tennyson (1988) demonstrated that a surface slick can be successfully detected from a distance of 5 km by using a shipborne X-band radar. Fingas and Brown (1997) indicated that shipborne radar successfully detected a surface slick from 8 km away. These results suggest that the operating range of an X-band radar for surface slick detection is approximately 5–8 km. Forget and Brochu (1996) used an X-band radar to measure currents and then predict oil-spill movements. Remote sensing of oil spills has become an integral part of oil-spill response around the world. However, oil-slick detection using radar is limited by the sea state. Very weak winds cannot produce sufficient sea clutter in the surrounding sea, and very high seas scatter the radar, blocking detection inside the wave troughs. The most suitable wind speeds for oil detection using the radar are 1.5–10 m/s (Fingas and Brown, 2014).

A fast oil-spill forecasting system is required for the mitigation of oil-spill disasters. Therefore, in this study, a two-step strategy for tracking oil-spill movements is proposed. First, an X-band radar is established to monitor oil spills at the earliest stage of the oil-spill event. The obtained location and extent of oil spill are then used as the initial conditions for the forecasting of oil-slick trajectories. Second, the core part of the SCHISM modeling system is applied to predict the water surface elevation and current speeds. After obtaining the associated hydrodynamic parameters, the Lagrangian particle-tracking method is used to forecast the trajectories of oil spills. The T. S. Taipei's oil-spill event is used as a case study for testing the capability of the proposed oil-tracking strategy, especially in the coastal waters. To verify the accuracy of the SCHISM, the simulated water surface elevations are compared with those obtained from a nearby tide station. The simulated surface currents are compared with the monitoring data collected from an HFR station of Taiwan Ocean Radar Observing System (TOROS). Following these verifications, simulations for coastlines fouling at the Shimen coast under various scenarios are compared with the observed situations.

2. SCHISM

The complete SCHISM is shown in Fig. 1. The core part of the SCHISM involves the use of hydrodynamic models to determine the water surface elevation and current (Zhang et al., 2016). The SCHISM is derived from the original semi-implicit Eulerian-Lagrangian finite-element (SELFE) model and has the following new features: (i) a highly flexible hybrid coordinate system in the vertical direction; (ii) unstructured triangular-quadrangular grids in the horizontal direction; and (iii) an implicit advection scheme for transport (Zhang and Baptista, 2008; SCHISM, 2016). Spurious flow due to pressure gradient errors (Haney, 1991) is a major challenge in ocean modeling. The SCHISM employs a new hybrid vertical coordinate of localized sigma coordinates with shaved cell (LSC^2) to alleviate this problem (Zhang

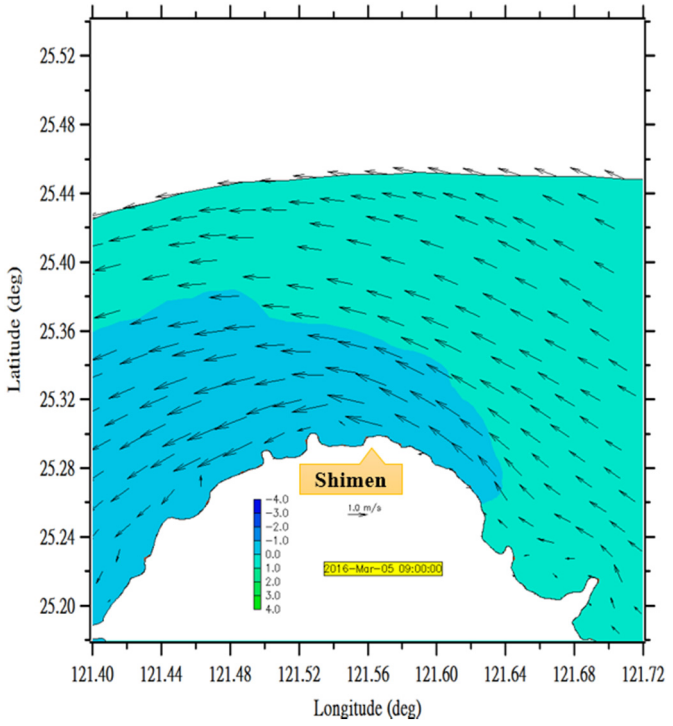

Fig. 9. Surface currents near the Shimen coast at 09:00 AM on March 5, 2016, predicted using the SCHISM. Colors indicate water surface elevation.

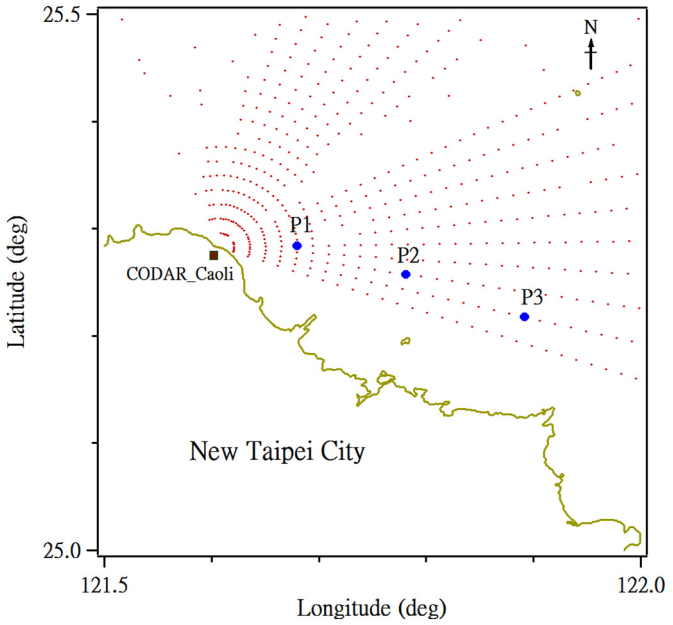

Fig. 10. Observational region covered by the HFR (SeaSonde, CODAR) at the Caoli station. The sites labeled P1, P2, and P3 (blue dots) represent the places where the observed radial surface currents were selected for comparison with the simulated ones. (For interpretation of the references to color in this figure legend, the reader is referred to the web version of this article.)

et al., 2015). The SCHISM has been successfully applied to oceanic, coastal, intertidal estuarine, river, and lake areas with complex topography and geometry, and has been demonstrated to achieve high accuracy in physical and biological processes (Tomas et al., 2014; Yu et al., 2017; Schloen et al., 2017).

2.1. Hydrodynamic model

The hydrodynamic model in the SCHISM solves the three-dimensional continuity and momentum equations in Cartesian coordinates as follows:

Continuity equations in 3D and 2D depth-integrated forms are as follows:

$$\nabla\cdot\mathbf{u} + \frac{\partial w}{\partial z} = 0 \tag{1}$$

$$\frac{\partial \eta}{\partial t} + \nabla\cdot\int_{-h}^{\eta}\mathbf{u}dz = 0 \tag{2}$$

Under the assumption that the pressure is hydrostatic, the momentum equations can be expressed as:

$$\frac{D\mathbf{u}}{Dt} = \mathbf{f} - g\nabla\eta + \frac{\partial}{\partial z}\left(\nu\frac{\partial \mathbf{u}}{\partial z}\right) - \frac{1}{\rho_o}\nabla p_A - \frac{g}{\rho_o}\int_z^{\eta}\nabla\rho\, d\zeta + \nabla\cdot(\mu\nabla\mathbf{u}); \tag{3}$$

where

$$\mathbf{f} = -f\ \mathbf{k}\times\mathbf{u} + \alpha g\nabla\psi \tag{4}$$

$\frac{D}{Dt}$: material derivative

∇: $\left(\frac{\partial}{\partial x}, \frac{\partial}{\partial y}\right)$

(x,y): horizontal Cartesian coordinates (m)

z: vertical coordinate, positive upward (m)

t: time (s)

$\mathbf{k}$: unit vector in the z direction

$\eta(x,y,t)$: free-surface elevation (m)

$h(x,y)$: bathymetric depth (m)

$\mathbf{u}(x,y,z,t)$: horizontal velocity, with Cartesian components (u,v) (ms^{-1})

w: vertical velocity (ms^{-1})

f: Coriolis factor (s^{-1})

g: acceleration due to gravity (ms^{-2})

ψ: Earth-tidal potential (m)

α: effective earth-elasticity factor (=0.69)

ρ_o: reference value of seawater density; by default it is set as 1, 025 (kg m^{-3})

ρ: seawater density, which is a function of pressure, salinity, and temperature

$p_A(x,y,t)$: atmospheric pressure at the free surface (N m^{-2})

ν: vertical eddy viscosity (m^2s^{-1})

μ: horizontal eddy viscosity (m^2s^{-1})

Determination of the salinity and temperature is necessary because they affect the density of the seawater along with pressure. The salinity and temperature of the seawater are determined from the transport equations:

$$\frac{DS}{Dt} = \frac{\partial}{\partial z}\left(\kappa\frac{\partial S}{\partial z}\right) + F_S \tag{5}$$

$$\frac{DT}{Dt} = \frac{\partial}{\partial z}\left(\kappa\frac{\partial T}{\partial z}\right) + \frac{\dot{Q}}{\rho_O C_P} + F_h \tag{6}$$

where

S, T: salinity and temperature of the water (practical salinity units (psu), $^{\circ}C$)

κ: vertical eddy diffusivity for salinity and temperature (m^2s^{-1})

F_S, F_h: horizontal diffusion and mass sources/sinks for transport equations

$\dot{Q}$: rate of absorption of solar radiation (Wm^{-2})

C_P: specific heat of water ($J\ kg^{-1}K^{-1}$)

The differential Eqs. (1)–(3) and (5)–(6) require initial and boundary conditions. In general, all state variables, such as (η, $\mathbf{u}$, S, T), are specified at $t = 0$ as the initial conditions and specified at all open boundary segments as the boundary conditions. At the sea surface, the

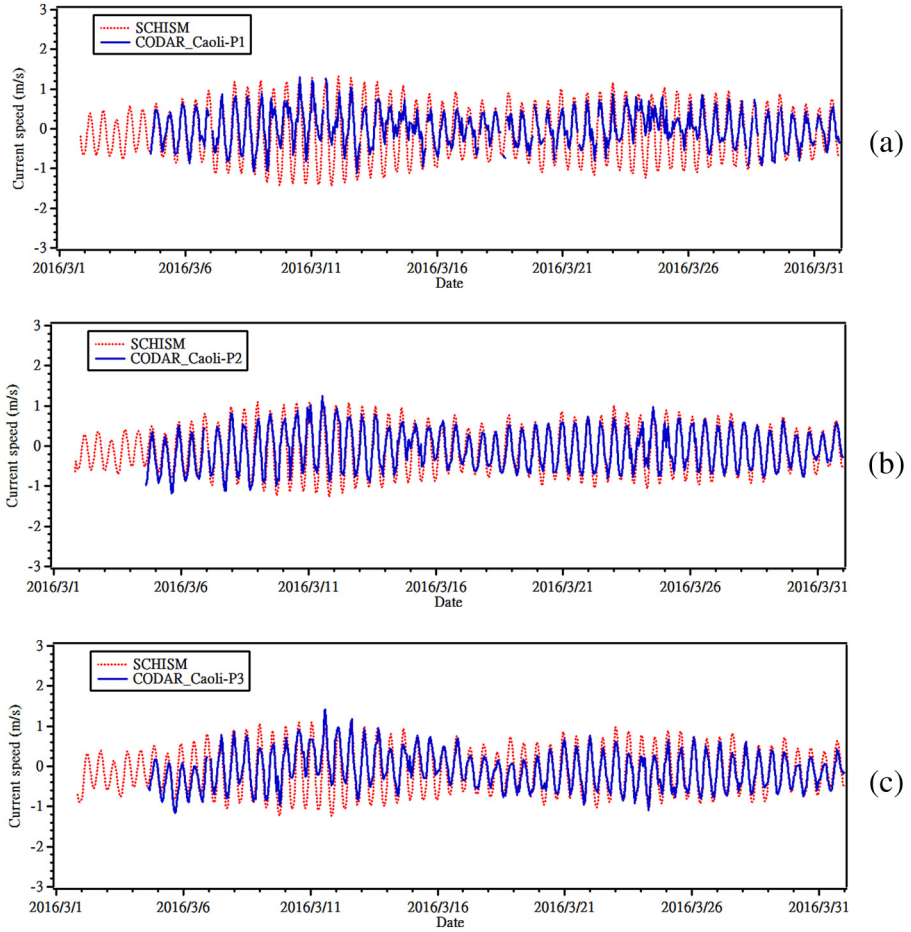

Fig. 11. Comparison of the simulated (red dashed line) and observed (blue solid line) radial surface current speeds near the Shimen coast in March 2016 at (a) P1, (b) P2, and (c) P3. (For interpretation of the references to color in this figure legend, the reader is referred to the web version of this article.)

SCHISM enforces the balance between the internal Reynolds stress and applied shear stress τ_w on the sea surface:

$$\nu\frac{\partial u}{\partial z} = \tau_w, \text{ at } z = \eta \tag{7}$$

The SCHISM incorporates the bulk aerodynamic module introduced by Zeng et al. (1998) to simulate the air-sea interaction and provides the values of τ_w.

In ocean models, the bottom boundary layer is usually not well resolved; hence, the no-slip condition at the sea bottom is replaced by a balance between the internal Reynolds stress and the bottom frictional stress,

$$\nu\frac{\partial u}{\partial z} = \tau_b, \text{ at } z = -h \tag{8}$$

The bottom shear stress τ_b depends on the type of boundary layer, which is assumed to be a turbulent boundary layer in the SCHISM. For turbulence closure, the generic length scale model of Umlauf and Burchard (2003) was adopted, which has the advantage of encompassing most 2.5-equation closure models (Mellor and Yamada, 1982; Rodi, 1984; Wilcox, 1998). For the details of the applied boundary conditions and turbulence modeling in the SCHISM, refers to SCHISM v5.3.1 Manual (SCHISM, 2016).

2.2. Lagrangian particle tracking

The SCHISM comprises two oil models for simulating oil spills: a simple Lagrangian particle-tracking method (particle-tracking gear is shown in Fig. 1) and a tracer transport-based model (VELA-OIL) developed by the National Laboratory of Civil Engineering, Portugal (Azevedo et al., 2014). For simplicity, the Lagrangian particle-tracking method for predicting oil spills is adopted in this study. In this model, spilled oil is represented as a group of particles and each particle is tracked independently. The movement of each particle is governed by the advection and diffusion processes, which are based on the advection-diffusion equation. The advection term involves the effect of current and wind velocities as well as the rising velocity of the oil slick due to buoyancy. The diffusion term describes the effect of random turbulent velocity. The Lagrangian particle-tracking method in the SCHISM includes the random displacement model (RDM), which is similar to the random walk model. However, the RDM is more accurate in heterogeneous media because the spatially non-uniform turbulent diffusivity is considered (Visser, 1997; North et al., 2006, 2011). The particle movement in RDM is represented as follows:

$$X^{n+1} = X^n + \left(U + W_x + \frac{\partial K_x}{\partial x}\right)\Delta t + R\sqrt{6K_x\cdot\Delta t} \tag{9}$$

$$Y^{n+1} = Y^n + \left(V + W_y + \frac{\partial K_y}{\partial y}\right)\Delta t + R\sqrt{6K_y\cdot\Delta t} \tag{10}$$

$$Z^{n+1} = Z^n + \left(W + V_r + \frac{\partial K_z}{\partial z}\right)\Delta t + R\sqrt{6K_z\cdot\Delta t} \tag{11}$$

where U, V, and W are the water velocity components in the Cartesian coordinates x, y and z, respectively; n is the current time step and $n + 1$ is the next time step; Δt is the time step interval; R is a uniform random number between -1 and 1; K_x, K_y, and K_z are turbulent diffusion coefficients in the x, y and z directions, respectively; and W_x and W_y are

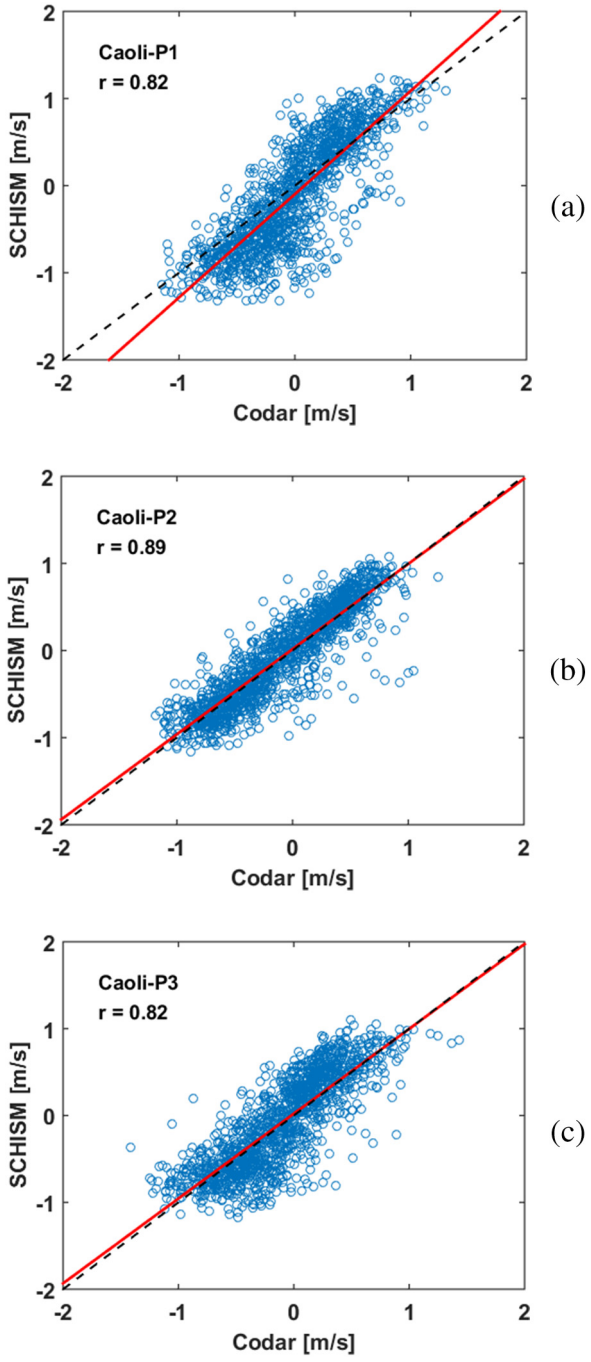

Fig. 12. Correlation between the simulated and observed radial surface current speeds at (a) P1, (b) P2, and (c) P3. The dashed black line indicates the perfect linear correlation with $r = 1.0$ and the solid red line indicates the actual correlation. (For interpretation of the references to color in this figure legend, the reader is referred to the web version of this article.)

Table 1
Statistical evaluation of model performance for surface current velocities at the Shimen coast.

Location	RMS error (m/s)	Correlation coefficient
P1	0.38	0.82
P2	0.24	0.89
P3	0.31	0.82

the wind dragging speeds in the x and y directions. Moreover, $W_i = c_d \times W\_vel_i^{10} (i = x \text{ or } y)$, where c_d is a dragging coefficient, typically 0.03, and $W\_vel_i^{10}$ refers to the wind velocity at 10 m above mean sea level. V_r is the rising velocity of the oil slicks due to the buoyancy, which can be determined from the following empirical equation (Clift et al., 1978; Zheng and Yapa, 2000).

$$V_r = \left[\frac{8}{3} g d_{oil} \left(1 - \frac{\rho_{oil}}{\rho}\right)\right]^{\frac{1}{2}} \tag{12}$$

where g is the acceleration due to gravity, d_{oil} is the oil droplet diameter, and ρ_{oil} and ρ are the density of oil and seawater, respectively.

When the oil particles reach the shoreline, the oil-shoreline interaction typically varies with oil properties (e.g., viscosity) and shoreline morphology. Several models have treated the oil-spill fate in the nearshore region (Gundlach et al., 1985; Reed and Gundlach, 1989). Reed and Gundlach (1989) addressed the oil-shoreline interaction for various shorelines and represented methods for quantifying the amount and residence times of oil on the shoreline. However, to the knowledge of the authors, little information exists regarding the stranded percentage of oil spills on various shorelines. In this study, it is assumed that 80% of oil particles that reach the land boundary are stranded and that the remaining 20% move off the shoreline. Sensitivity tests have revealed that the extent of the fouled coastline does not change much when the stranded percentage changes from 80% to 40%. The stranded oil particles may be refloated on a rising tide. The particles that cross the open boundary are assumed to leave the computational domain and not return. Thus, the modeling region must be sufficiently large compared to the area of interest.

3. Remote sensing of oil spill using land-based X-band radar

The original nautical X-band radar can detect objects that induce strong radar backscattering. Accordingly, the patterns of gravity waves, ship, and land may appear on the radar image and affect the identification of oil spills. In this paper, we propose a series of steps for radar image processing for detecting oil spills. The main purpose of image processing is to identify the area with low echo intensity due to oil spills. Fig. 2 shows the proposed procedure of oil-slick detection by using nautical radar images. As shown in Fig. 2, the first step is to eliminate the ocean wave patterns by taking a time average of continuous radar image sequences. The patterns of gravity waves are often obvious because of strong backscattering from the wave crests and the effects of wave shadowing (Nieto Borge et al., 2004). Accordingly, the patterns of sea surface waves or swells can be eliminated by taking a time average of radar image sequences $f(t, r, \theta)$ as follows:

$$g(r, \theta) = \frac{1}{N_t} \sum_{t=1}^{N_t} f(t, r, \theta) \tag{13}$$

where $g(r, \theta)$ denotes the time-averaged radar echo intensity at different distances r and azimuths θ from the radar antenna. In this study, 128 continuous radar image sequences ($N_t = 128$) taken within every 30 min were averaged.

Because the radar echo intensities are values relative to the transmitted power, there is no quantitative relationship between echo intensity and sea surface features. In the second step, we normalize $g(r, \theta)$ by dividing it with respect to its maximum value, G, within the domain:

$$g'(r, \theta) = g(r, \theta)/G \tag{14}$$

where $g'(r, \theta)$ is referred to as the normalized time-averaged radar echo intensity.

The oil slicks are detected by identifying the area with a low radar echo intensity. However, the geometrical spreading of the propagating radar waves will also cause a spatial decrease in the radar wave intensity, which in turn results in a spatial decay of the radar echo intensity. Theoretically, the decay of radar echo intensity is proportional

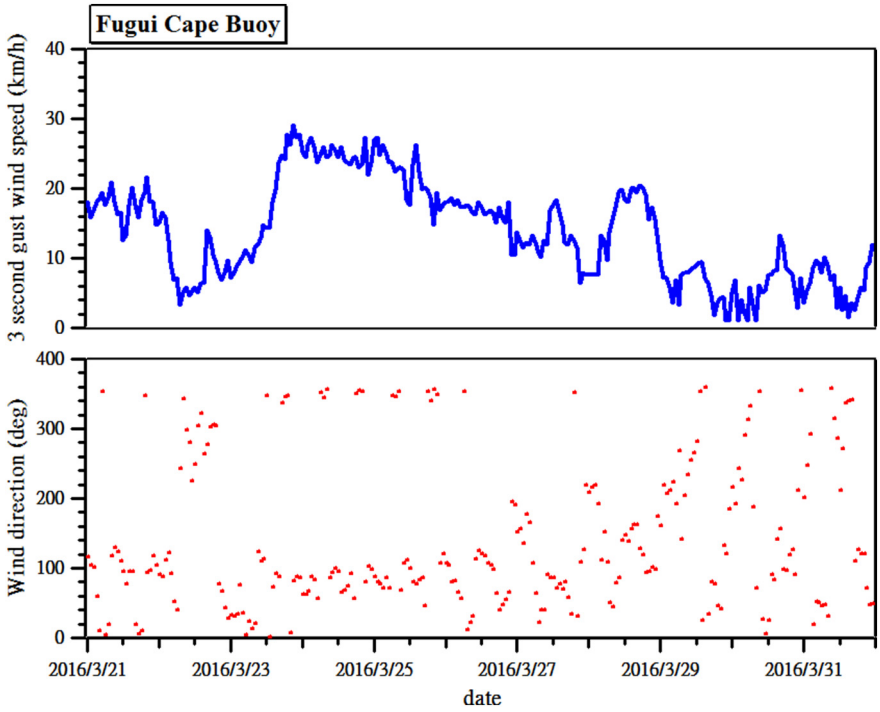

Fig. 13. 3-s gust wind speed (top) and wind direction (bottom) obtained from the Fugui Cape buoy from March 21 to 31, 2016.

to r^{-4} (Kanevsky, 2008). However, in real situations, the decay of radar echo is also affected by environmental factors such as the grazing angle, sea surface roughness, and atmospheric compositions. Accordingly, in the third step, the decay of echo intensity with distance from the antenna is determined. This information is then used to remove the spatial decay effect to obtain the actual echo intensity. To reveal the decay behavior of radar echo intensity with distance, we first take a spatial average of $g'(r,\theta)$ in the azimuthal direction as follows:

$$h'(r) = \frac{1}{N_\theta} \sum_{\theta=\theta_a}^{\theta_b} g'(r,\theta) \tag{15}$$

where θ_a and θ_b are the lower and upper bounds of azimuth in $g'(r,\theta)$ and N_θ is the total number of bins inside the azimuth range. To overcome the influence of noise on the evaluation of the decay of the echo intensity with distance, Eq. (15) is applied only to the radar observation area without any ship or land. In Eq. (15), $h'(r)$ represents a radial echo intensity function. To obtain a compact range of the radial echo intensity, we take the natural logarithm of Eq. (15):

$$h(r) = \log_e[h'(r)] \tag{16}$$

The results obtained from Eq. (16) are shown in Fig. 3. The radial echo intensity $h(r)$ decays continuously with distance; however, $h(r)$ is not so smooth such that a representative function for it can be easily determined. Therefore, we use the ensemble empirical mode decomposition (EEMD) method. The EEMD method decomposes the signals into different components called intrinsic mode functions (IMFs) (Wu and Huang, 2008). After eliminating all IMFs from the signals, the final residue $T(r)$ is usually a monotonic function. The final residue should correspond with the trend of the data (Huang et al., 1998). We used $T(r)$ to represent the radial echo intensity function $h(r)$as shown in Fig. 3. To obtain the true normalized echo intensity without the decay effect due to the distance, we correct $g'(r,\theta)$ using $T(r)$. The corrected (true) normalized echo intensity $C(r,\theta)$ is then determined as follows:

$$C(r,\theta) = g'(r,\theta) \times [e^{T_{\max}}/e^{T(r)}] \tag{17}$$

where $T_{\max}$ is the maximum of $T(r)$. Notably, when $T(r)$ equals $T_{\max}$, $C(r,\theta) = g'(r,\theta)$. The oil-spill areas are identified as the areas where $C(r,\theta)$ is low.

To avoid false identification of the oil-spill pattern, in the fourth and fifth steps of radar image processing, the areas without the possibility of oil spills are marked. In our case, the land, ship, and sea surface behind the ship are all marked as the impossible areas for oil slick. The marked areas are excluded in the identification of the oil slick. The radar echos from the sea surface behind the ship are restrained because of the shadowing effects of the hull. In the case of oil leaks in this sea area, it will not be detected.

The last step of image processing is to identify the areas with low echo intensities. Hence, a threshold value is required. The easiest method is to determine a threshold value subjectively. However, the subjective threshold greatly depends on the experience of the decision maker. To avoid errors in the evaluation of oil-spill images, we adopt the Otsu method (Otsu, 1979), which can automatically select a suitable threshold from gray-level histograms. Liu et al. (2017) used the Otsu method to successfully determine the oil-spill area from marine radar images. To apply the Otsu method, the radar image is assumed to contain two classes of pixels, and their echo intensities can be described using a bi-modal histogram. Ideally, these two classes represent the oil area and non-oil area. The optimum threshold can separate these two classes so that their combined spread is minimal. That is, we exhaustively search for a threshold that minimizes the weighted sum of variances of the two classes. The Otsu method yields favorable performance if the histogram of the radar echo intensities is bimodal. If the image is corrupted by strong noise, the bimodal histogram is unclear. Then, the Otsu method may not determine a suitable threshold value and result in errors in oil pattern detection. We continuously monitor the sea surface around the grounded ship. If the ship starts to leak oil or when the oil spills onto the sea surface, the echo intensity of the oil-spilled areas becomes weaker. Consequently, we can identify the location and extent of the oil spills.

Fig. 4 shows the field operation of oil-spill monitoring by setting up an X-band radar at the coast near the grounded container ship, T. S. Taipei. The X-band radar system can be set up and put to work within half an hour. In this study, we collect a series of 128 radar images at intervals of 30 min for further data analysis. We arrived at the nearby

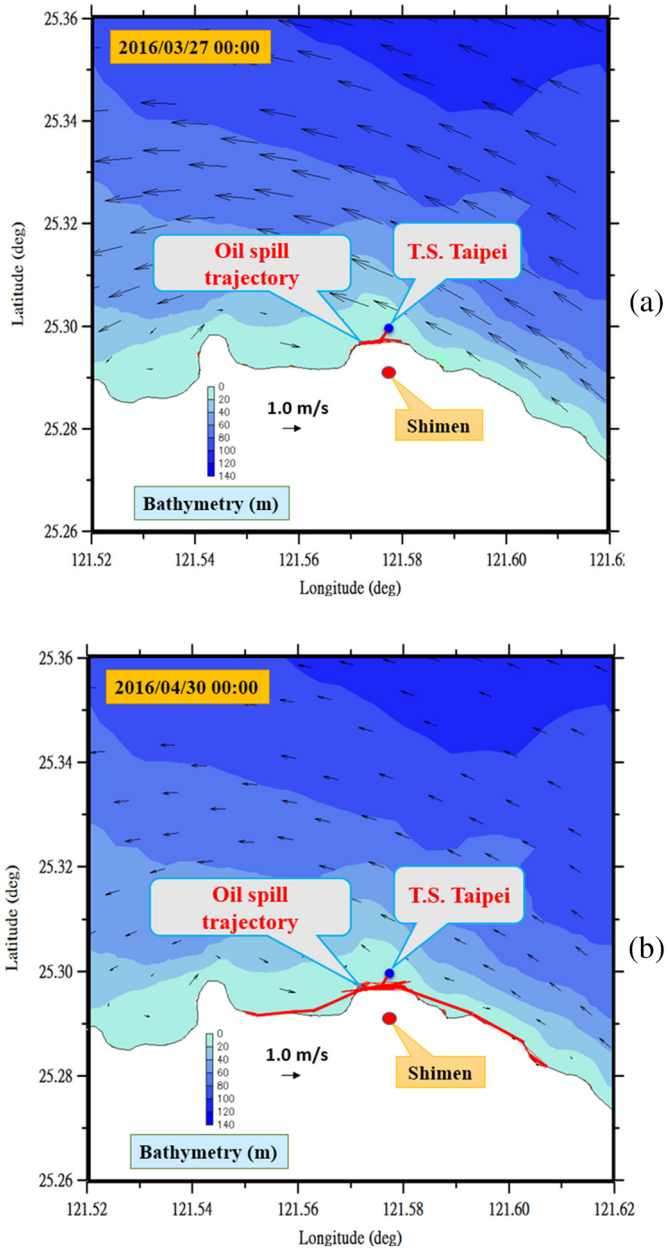

Fig. 14. Model-simulated surface oil-slick trajectory after occurrence of the oil spill at the Shimen coast over (a) 1 day and (b) over 34 days. The oil partciles were released at 00:00 AM on March 26, 2016, from the location of the stranded ship, and the 3-s gust wind speeds obtained from Fugui Cape buoy were adopted. The color represents bathymetric depth.

coast on March 14, 2016, and at the beginning of monitoring, no oil leak from the ship was detected. However, as wave heights increased, the ship eventually broke, causing the oil to leak into the sea. Fig. 5 shows the results of oil-slick identification based on the image processing shown in Fig. 2. The oil-slick information contained in Fig. 5 can be used as the initial conditions for the forecasting of subsequent oil-spill trajectories.

4. Proposed oil-spill forecasting based on the SCHISM and X-band radar

This paper proposes a two-step strategy for tracking the trajectories of oil spills. First, an X-band radar is set up to monitor oil spills. If the oil spills occur on the open seas, the radar images of oil spills can be obtained from the navigation X-band radar installed on the ship. Moreover, radar images for oil spills occur in coastal areas can be obtained by setting up an X-band radar at the nearby coast. Multi-temporal imaging captured by the X-band radar can provide the oil-spill location and extent. Subsequently, the trajectory of an oil spill in the coastal regions can be quickly estimated using the surface currents, which can also be obtained from the X-band radar. The oil-spill forecasting in the first step enables response operation for the rapid dispatch of emergency equipment. The location and extent of oil spills obtained from the X-band radar can also be used as the initial condition for the subsequent prediction of oil-spill trajectories.

Generally, oil-slick movement can be estimated from the vector sum of the wind and current velocities. The windage factor, which provides the transport speed of oil, is typically 3% of the wind speed, based on analytical derivation and empirical observation (Stolzenbach et al., 1977). Moreover, oil slicks generally move at a rate of 100% of the surface current and approximately 3% of the wind speed. The 3% rule represents average conditions. The actual windage factor ranges from 1% to 6% (Lehr and Simecek-Beatty, 2000; Simecek-Beatty and Lehr, 2007), or from 1% to 4% (Zelenke et al., 2012), or from 0% to 6% (Beegle-Krause, 2018). This factor depends on the densities of oil masses and usually decreases over time due to oil weathering (Beegle-Krause, 2018). In the open sea, the wind largely influences oil-slick movement if the wind speed exceeds 20 km/h (Fingas, 2014a). In most cases, the major limitation for accurately predicting oil-slick movement is a lack of reliable wind speed estimates. The accuracy of the wind forecast depends on factors such as special weather features, the length of the forecast period, and ability to localize the prediction to the spill site. Optimal forecast periods are usually from 6 to 24 h. Moreover, the resolution of the atmospheric model plays also a critical role. For most cases, regional mesoscale (10–50 km) models are suitable for oil-spill trajectory modeling. But even with regional models, the sea breeze may not be sufficiently resolved. This can produce a large error in a trajectory forecast (Simecek-Beatty, 2011). Winds as light as breezes can lead to oil beaching (Beegle-Krause, 2018).

Because the hydrodynamic scale in the coastal region is usually small and varies quickly, the hydrodynamic model is critical for obtaining information on water surface elevations and coastal currents. Accordingly, the SCHISM is used to determine hydrodynamic parameters such as the water surface elevations and currents. The wind data that are also required for predicting the oil-spill trajectories can be obtained from various ways as will be discussed in the next section. The Lagrangian particle-tracking method included in the modeling system is then used to simulate the trajectories of oil slicks after the surface current and wind data are available and the initial location of oil spill is known.

5. Case study of an oil-spill event

5.1. T. S. Taipei oil spill

The container ship T. S. Taipei ran aground on March 10, 2016, at the location with coordinates 25° 18′ 3.87″ N, 121° 34′ 36.60″ E, which is approximately 250 m off the Shimen coast. The Shimen coast is located in the northernmost part of Taiwan (Fig. 6) and is well known for harsh sea conditions with strong northeastern wind and high seas, especially during fall and winter. The Shimen coast is also a popular tourist attraction for its diversity in landforms and beaches, such as the rocky shore and headland, sea caves, wave-cut platform, algal reef, and shell sand beach. On March 11, the following day, cracks were found in the ship hull, and oil began to leak. On March 25, the ship broke into two parts, and approximately 50 tons of fuel oil leaked into the sea during the morning of March 26, 2016. Countermeasures for rescuing the grounded ship and cleaning up the spilled oil were immediately taken by the EPA, Taiwan. These countermeasures included removal of the remaining oil in the ship by suction, deployment of oil booms to

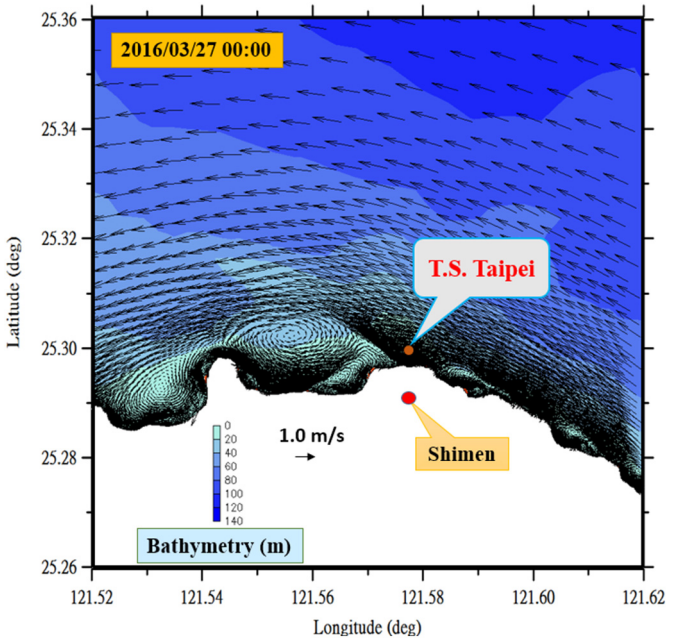

Fig. 15. Detailed flow fields that correspond to those in Fig. 14 (a). The flow fields were obtained based on the computational mesh shown in Fig. 7. The color represents bathymetric depth. (For interpretation of the references to color in this figure legend, the reader is referred to the web version of this article.)

control the oil spills, and placing sponges on the surface of the spill-affected area to suck and absorb the oil from the water surface. The fouled rocky coasts were cleaned by using strong hot water. These countermeasures for cleaning up oil spills are rather conventional; more effective and environmentally friendly ways are expected in the future (Freudenburg and Gramling, 2011; Lin and Kao, 2016). Because of the harsh weather these countermeasures were performed intermittently. According to the report of EPA Taiwan (2016) and Huang et al. (2016), oil-spill cleanup at sea was complete on May 3, 2016, and shoreline cleanup was complete on May 10, 2016.

We arrived at Shimen coast first on March 11, 2016, at which point no oil leaks from the ship were observed. We revisited the Shimen coast on March 26, 2016, and began to monitor the oil spills by setting up an X-band radar at the nearby coast (Fig. 4). Fig. 5 shows the distribution of surface oil slicks obtained using the radar set up at the Shimen coast at 09:00 AM (Local Time), on March 26, 2016. The oil slicks are shown as dark features in the X-band radar images. The extent and location of the oil spills can be used as the initial condition for predicting the consequent oil-spill trajectories.

5.2. Prediction and verification of water level and current

When oil spills on water, most oil spreads quickly, forming a thin film. Subsequently, the oil is advected by winds and currents. Consequently, both current and wind data are crucial for the prediction of oil trajectories. The SCHISM is used to predict the water level and current as well as the trajectories of oil slicks. Therefore, in this study we form an unstructured triangular mesh near the Shimen coast (Fig. 7). The computational mesh comprises 118,132 elements, with a horizontal resolution of approximately 2 km on the open boundary and a minimum horizontal resolution of 15 m on the land boundary. The water depth varies from approximately 270 m in the open sea to approximately 3 m in the coastal areas. The open boundary conditions for elevation, the vertical profile of horizontal velocities, temperature, and salinity are derived from the HYbrid Coordinate Ocean Model (HYCOM). The HYCOM is a global ocean prediction model designed for

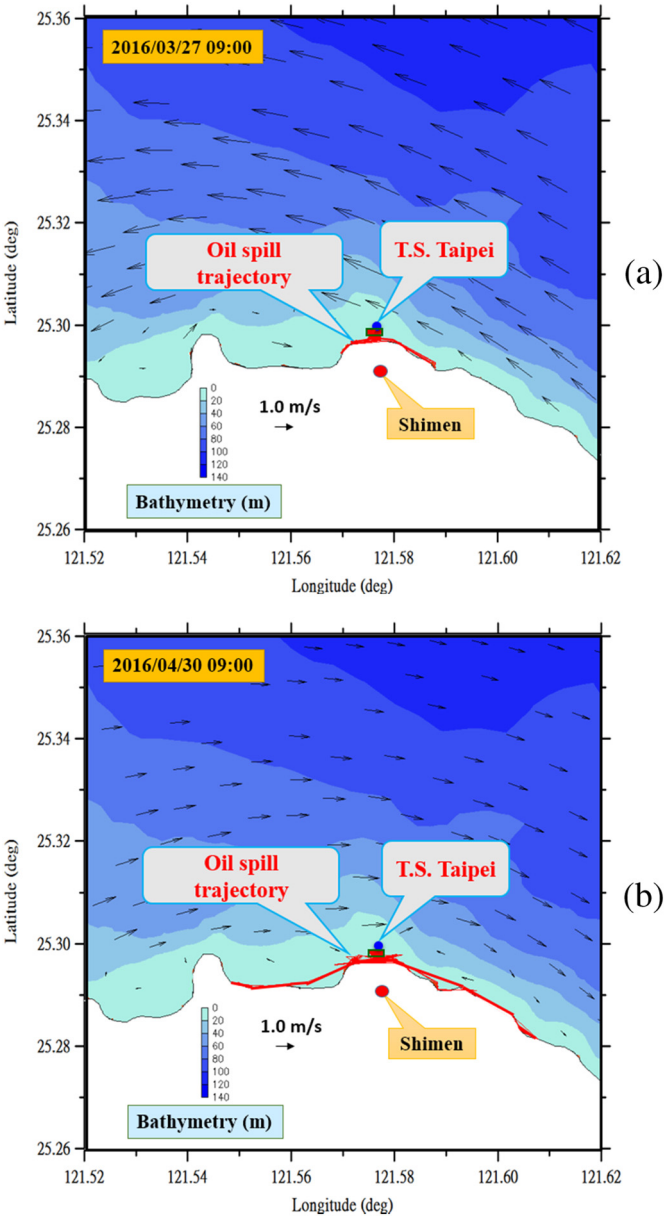

Fig. 16. Model-simulated surface oil-slick trajectory after the oil spill occurred at the Shimen coast over (a) 1 day and (b) 34 days. The monitored oil-spill area obtained from the X-band radar at 09:00 AM on March 26, 2016, was used as the initial locations of the oil spills, and the 3-s gust wind speeds obtained from Fugui Cape buoy were adopted. The color represents bathymetric depth. The area of initial oil slick is represented as a rectangle with a length of 218 m and a width of 42 m.

the United States Global Ocean Data Assimilation Experiment. The resolution in the HYCOM is 1/12°, which corresponds to a distance of 9.26 km.

Initial conditions at the computational surface, including air pressure, wind field, surface shortwave radiation heat flux, and specific humidity, are obtained through interpolation of the results obtained using the weather research and forecast (WRF) model developed by the Central Weather Bureau (CWB), Taiwan. Moreover, the wind wave model (WWM) is incorporated into the SCHISM for assessing the effect of surface waves; however, the results show only minor differences from those without WWM.

To verify the accuracy of the SCHISM, we first compared the simulated time series of the water surface elevation with the observed ones at the Linshanbi tidal station from March 1 to March 31, 2016. The

Fig. 17. Extent of oil slick on the coastline obtained from EPA (Taiwan) during the period from March 26, 2016 to May 10, 2016. The brown color represents the oil fouled coastline (replotted based on the information from Huang et al. (2016)). (For interpretation of the references to color in this figure legend, the reader is referred to the web version of this article.)

comparison was shown in Fig. 8. The Linshanbi tidal station is located approximately 6.8 km away from the container ship, T. S. Taipei, as shown in Fig. 6. Fig. 8 shows a close agreement between the simulated and observed water elevations.

To verify the accuracy of the simulated current speed, we collected radial current velocity data from the Caoli station of the TOROS. This system consists of 18 HFR stations and adopts the SeaSonde (CODAR Ocean Sensors, Santa Cruz, CA, USA) to monitor the sea surface currents around Taiwan Island. The HFR network product is useful for providing essential information on ocean surface currents (Fredj et al., 2017). The Caoli station is located at the northern coast of Taiwan and is approximately 3.5 km away from the T. S. Taipei grounding site (Fig. 6). Fig. 9 displays the model-predicted surface currents near the Shimen coast at 09:00 AM on March 5, 2016. Black arrows denote the surface current velocity, with longer arrows indicating faster current speeds. The color bar indicates the corresponding water surface elevations for different colors. Fig. 9 shows that the simulated surface currents are roughly parallel to the coastline. This is consistent with the known facts that the main current component along the coasts of Taiwan is the tidal current, which is usually parallel to the coastline (Wang et al., 2003; Tsai et al., 2016). Fig. 10 shows the monitored area covered by the Caoli HFR station. Sites labeled as P1, P2, and P3 (blue dots) were the locations where the observed radial surface current speeds were selected for comparison with the simulated ones. The small dots in Fig. 10 represent the locations of the available current data from the Caoli station. Fig. 11 (a)–(c) compare the simulated radial surface current speeds from March 1 to 31, 2016, obtained from the SCHISM with those obtained from the Caoli station at P1 to P3, respectively. The distances between the Shimen coast, the Caoli station, and the locations of P1-P3 can be read out from Fig. 6. Notably from Fig. 11 that the simulated radial surface current speeds are in close agreement with the observed ones, especially at the P2 location. The differences in the current speeds may be associated with the numerical errors of the SCHISM or the rougher resolution involved in the CODAR measurements. The resolution in the CODAR measurements is 1.5 km, whereas in the computation the grid size ranges from 15 m on the land boundary to 2 km on the open boundary. However, the overall consistency between the simulated and observed currents is strong.

A correlation coefficient is a statistical measurement to indicate how one variable changes with respect to another. The most common measure of correlation in statistics is the linear correlation coefficient r which measures the strength and direction of a linear relationship between two variables, and is determined as follows.

$$r = \frac{n\sum xy - (\sum x)(\sum y)}{\sqrt{n(\sum x^2) - (\sum x^2)}\sqrt{n(\sum y^2) - (\sum y^2)}} \tag{18}$$

where x and y denote the two variables and n is the total number of the variable. The range of r is between -1 and $+1$. The $+$ and $-$ signs indicate positive and negative linear correlations, respectively. If x and y have a strong positive linear correlation, r is close to $+1$. A correlation greater than 0.8 is generally described as strong, whereas a correlation less than 0.5 is generally described as weak (Montgomery and Runger, 2010).

Fig. 12 (a)–(c) show the correlations between the simulated and observed radial surface current speeds at P1–P3 locations, respectively. The dashed black line indicates the perfect linear correlation with $r = 1.0$ and the solid red line indicates the actual correlation coefficient obtained using regression analysis. Table 1 summarizes the corresponding root-mean-square (RMS) errors in the radial surface velocity and correlation coefficients at three sites. The table shows that the RMS errors in the velocity are less than 0.38 m/s and the correlation coefficients vary from 0.82 to 0.89. These results demonstrate that the simulated surface currents obtained from the SCHISM correlate well with the monitoring data obtained from the Caoli HFR station.

5.3. Wind data

The wind data required for forecasting of the oil-spill trajectories can be obtained from various operational meteorological models such as (i) the Global Forecast System developed by the National Centers for Environmental Prediction; (ii) the atmospheric model high-resolution 10-day forecast by the European Weather Center; (iii) the unified model by the Met Office; (iv) the numerical weather prediction by the Japan Meteorological Agency; and (v) the weather research and forecasting by the CWB, Taiwan. In some cases, the wind fields may also be obtained from in-situ measurements. However, the wind observation data can be used only in hindcasting and not forecasting for the oil-spill trajectories.

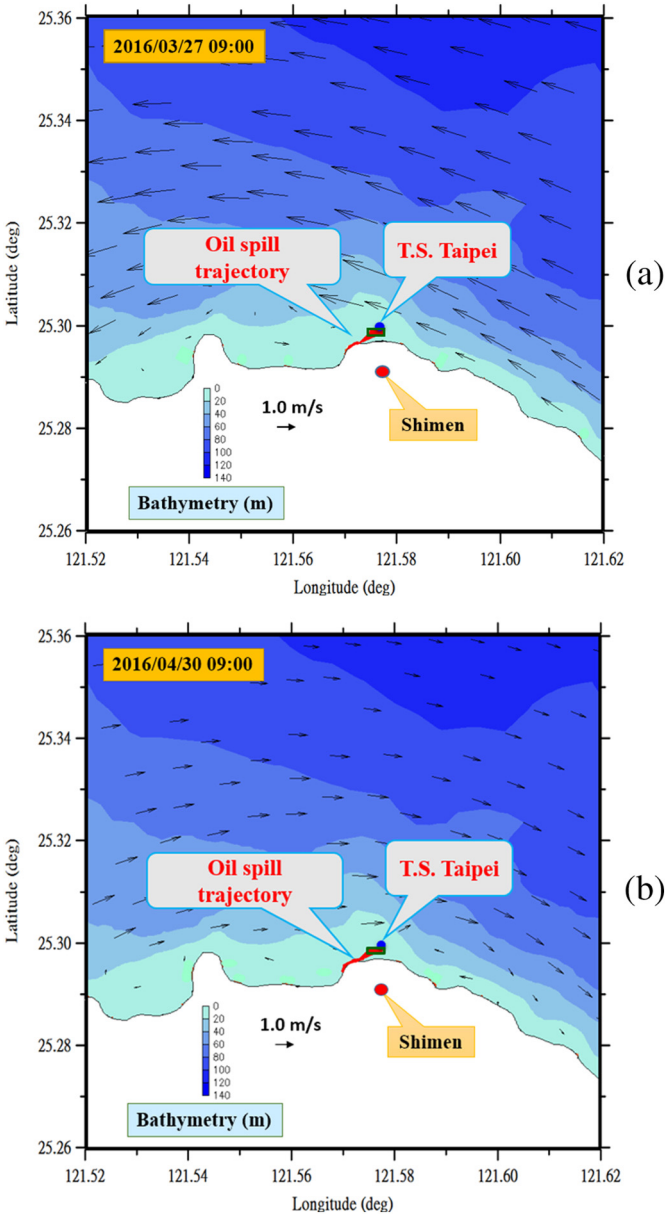

Fig. 18. Model-simulated surface oil-slick trajectory obtained under the same conditions as those used in Figs. 16 (a) and (b) except that the wind data were obtained from the WRF model.

In the forecasting of the oil-spill trajectories, this study used the Weather Research and Forecasting (WRF) model of CWB to forecast the wind. In the numerical simulation, the temporal resolution was 1 h, and the horizontal resolution was $5km \times 5km$. This horizontal resolution was finer than that used in the regional mesoscale models suited for oil-spill trajectory modeling, as mentioned in Section 4. The forecast period was 6 h. The WRF model solved the Euler non-hydrostatic equations for compressible flows and used the hybrid variational-ensemble data assimilation algorithm (Chen and Dudhia, 2000; Schwartz et al., 2013).

In the present case, local wind observation data are available from a nearby data buoy, referred to as the Fugui Cape buoy, which is located at the north of Fugui Cape (Fig. 6) and is approximately 4.2 km away from the stranded T. S. Taipei. This buoy belongs to the CWB, Taiwan, and is operated by the Coastal Ocean Monitoring Center, National Cheng Kung University, Taiwan. This buoy measures air pressure, air temperature, wind speed and direction, water temperature, wave height and direction, and current speed and direction. The measurements are conducted hourly, each with a duration of 10 min and a sampling rate of 2 Hz. The buoy provides hourly 3-s gust wind velocity and the mean wind velocity based on the 10-min data. Fig. 13 shows the 3-s gust wind speed and wind direction observed at the Fugui Cape buoy from March 21 to 31, 2016. Notably that the gust wind speed exceeded 20 km/h during March 23 to 25, 2016, indicating that during this period both wind and sea surface current were the critical factors affecting the movement of the oil slick. Fig. 13 shows that during March 23 to 27, 2016, the wind near the Fugui Cape was mainly northeasterly, ranging from 0° (north) to 90° (east).

Notably, the main current component along the coasts of Taiwan is the tidal current, which is usually parallel to the coastline (as mentioned in Section 5.2), whereas the wind speed and direction are usually seasonal and may depend on specific weather features, such as typhoons and tornadoes. The temporal variations in the wind speed and direction are much more extreme than those of the current speed and direction. These features can be noted by comparing the current data with the wind data for the Shimen coast area (Figs. 11 and 13). Thus, the winds are more likely to lead to erroneous oil beaching forecasts than the currents, especially for oil spills that are close to the coast.

5.4. Simulation and verification of oil-spill trajectories

After verifying the accuracy of the water surface elevations and current speed, we used the particle-tracking package in the SCHISM to simulate the movements of oil spills. Because local wind observation data are available, we adopt the 3-s gust wind data from the Fugui Cape buoy as the input wind data for simulating the oil-spill trajectories, and these data are updated hourly. Hindcasting of oil-spill trajectories is performed in two ways. In the first simulation, we assume that no information on the location and extent of oil spills is available and that the oil is released from the ship for 1 h with 1000 particles. Because the exact initial release time of oil slick is unknown, it is set to 00:00 AM on March 26, 2016, and the initial location is set to the coordinates of the stranded ship. The model is run with a time step of 120 s for two different periods, namely 1 day and to the end of April (34 days), because the cleanup of oil spills at sea was complete around this time. Fig. 14 (a) and (b) illustrate the model-predicted surface oil-slick trajectories at the Shimen coast over 1 day and 34 days, respectively. Fig. 14 (a) shows that after one day of oil leakage, the oil slicks drifted to the coastline of Shimen. The oil slick extended approximately from $(25.302^{\circ}N, 121.572^{\circ}E)$ to $(25.302^{\circ}N, 121.579^{\circ}E)$, which is approximately 780 m long along the coastline. Fig. 14 (b) shows that after 34 days, the length of fouled coastline increased to approximately 8 km, ranging roughly from $(25.298^{\circ}N, 121.553^{\circ}E)$ to $(25.288^{\circ}N, 121.608^{\circ}E)$. To enhance the clarity of the flow fields near the Shimen coast, Fig. 15 shows detailed flow fields that correspond to those in Fig. 14 (a). The flow fields were obtained based on the computational mesh shown in Fig. 7. Fig. 15 presents detailed flow fields, including the large and small circulations, near the coast. The flow fields near the coast are crucial for simulating the oil beaching.

In the second simulation, the information on the location and extent of oil spills obtained from X-band radar at 09:00 AM on March 26, 2016, (Fig. 5) is used as the initial condition. The initial area of oil slick is represented as a rectangle with a length of 218 m and a width of 42 m. The spilled oil is represented as a group of 1000 particles that distribute uniformly inside the rectangle, and each particle is tracked independently. The model is also run for 1 and 34 days, and the model-simulated oil-slick trajectories are shown in Fig. 16 (a) and (b), respectively. Fig. 14 (a) shows that after 1 day of oil leakage, the oil moved to the coastline. This is because of two factors: First, the wind direction during this period was mainly northeasterly. This wind drove the oil toward the coast. Second, the stranded ship was quite close to the coast. Therefore, the driven oil reached the coast within a short period. Comparing Figs. 16 (a) and 14 (a) reveals that the extent of the fouled coastline in Fig. 16 (a) is larger than that in Fig. 14 (a).

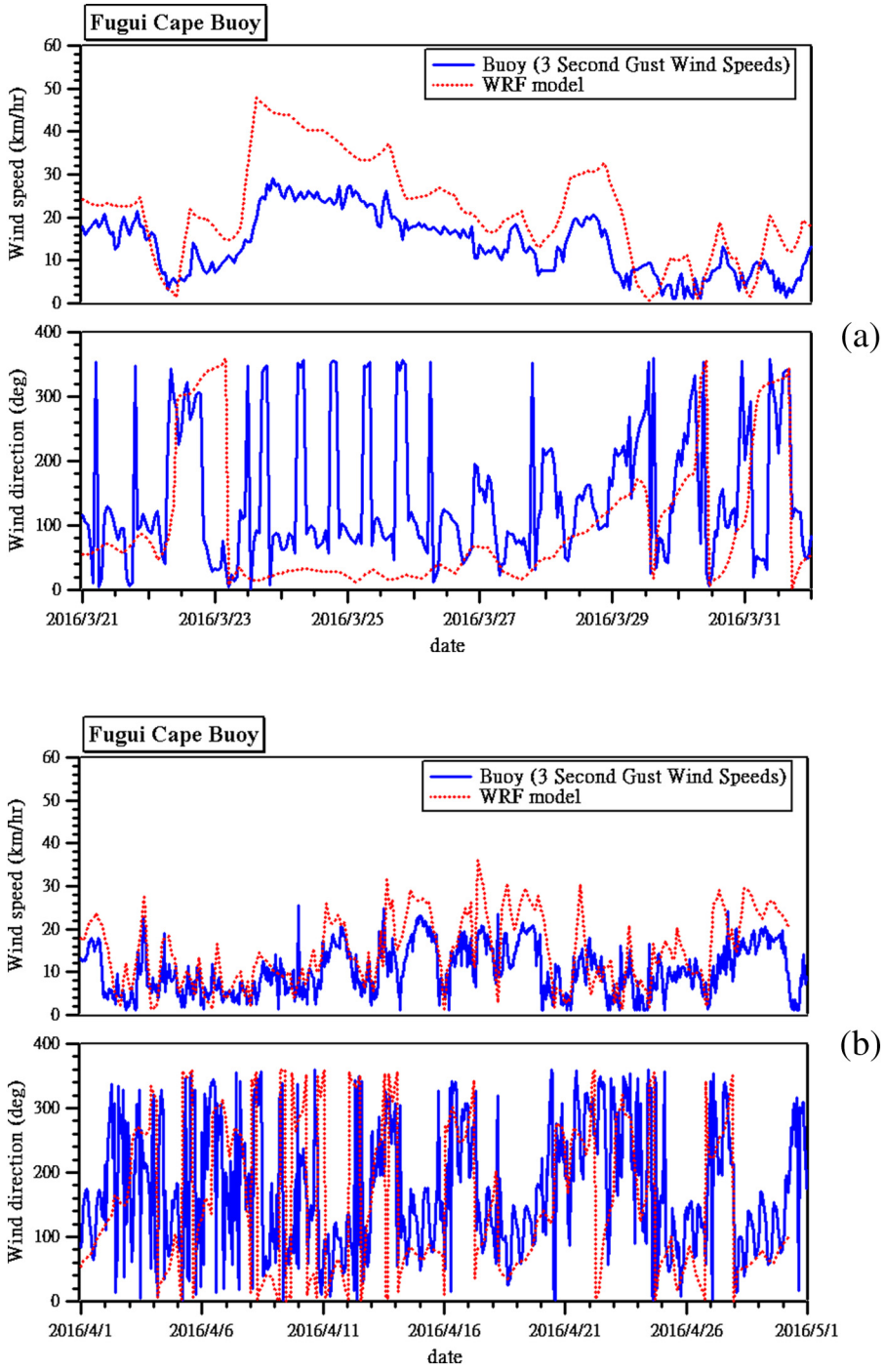

Fig. 19. Comparison of the simulated and observed wind speeds and wind directions at the location of Fugui Cape buoy on (a) March 21–31, 2016, and (b) April 1–30, 2016.

Factors that may cause wider shoreline oiling include the timing of the oil release with respect to the tides, the time period of release, and the initial extent of oil spills. From the tide data presented in Fig. 8, it can be noted that in both Fig. 14 (a) and 16 (a), the oil particles were released for 1 h during the rising tide. In Taiwan, tides originate from the western Pacific Ocean and are diffracted by the island of Taiwan. Consequently, the currents induced by the ebbing and rising tides at the Shimen coast (the northernmost part of Taiwan) run parallel to the coast and are in the opposite direction. Based on the aforementioned reasons, we suggest that the larger extent of fouled coastline in Fig. 16 (a) is associated with the larger initial extent of oil spills. However, this study provides only two test cases, which may be insufficient for exploring the causes of wider shoreline oiling.

According to the aerial photography carried out by the EPA, Taiwan, (EPA Taiwan, 2016) and Huang et al. (2016), the spilled oil spread across 9 km of the Shimen coast (Fig. 17). The model-simulated oil-slick trajectories shown in Fig. 14 (b) and 16 (b) are very similar to the observed one shown in Fig. 17. The extent of the foulded coastline shown in Fig. 16 (b) is more similar to that shown in Fig. 17 than that in Fig. 14 (b) because the oil slicks drifted more westward and were closer to the Fugui Cape; however, the difference is minor. The better results in Fig. 16 (b) should be attributed to the accurate initial condition of the oil-spilled area. Notably, some oil slicks in Figs. 14 (b) and 16 (b) do not move to the shore and remain there as observed in the real situation.

Table 2
Observed and predicted wind speeds and wind directions from 09:00 AM on March 26 to 09:00 AM on March 27, 2016.

Date	Time (hh:mm)	Observation		Model	
		Wind speed (km/h)	Wind direction (°)	Wind speed (km/h)	Wind direction (°)
March 26	09:00	16.56	31	27.14	41
	10:00	16.20	113	26.68	39
	11:00	18.00	125	26.28	36
	12:00	17.28	121	25.88	33
	13:00	16.20	118	25.60	31
	14:00	16.56	107	25.34	28
	15:00	16.92	104	25.13	25
	16:00	16.56	99	23.69	31
	17:00	15.12	64	22.46	37
	18:00	17.28	40	21.60	44
	19:00	15.84	48	21.02	52
	20:00	15.12	55	20.88	60
	21:00	18.00	66	21.06	67
	22:00	10.44	195	20.34	67
	23:00	10.44	191	19.58	67
March 27	00:00	13.68	152	18.86	67
	01:00	12.60	156	18.11	66
	02:00	11.52	136	17.39	66
	03:00	12.24	178	16.63	66
	04:00	11.88	165	16.52	59
	05:00	13.32	107	16.63	52
	06:00	12.24	64	16.99	45
	07:00	10.80	23	17.57	39
	08:00	10.08	41	18.36	33
	09:00	12.60	41	19.33	27

This error may result from the inaccuracy involved in the simulated current and wind speeds near the shore, or it may due to the calculation grid in this area. Some grids close to the shoreline are dry due to tidal effects. Therefore, the oil slicks on the dry grids do not move to the shore and remain as a close-to-straight line as shown in Figs. 14 (b) and 16 (b).

5.5. Forecasting of oil-spill trajectories

In the previous simulations of oil-spill trajectories, the available observation data for wind has been used. However, for the forecasting of oil-spill trajectories the wind data must also be predicted. This study used the WRF model of CWB to forecast the wind. Accordingly, the forecasting of the oil-spill trajectories based on the wind data obtained from the WRF model were performed under the same conditions as those used in Fig. 16 (a) and (b), and the corresponding results are shown in Fig. 18 (a) and (b). The fouled coastlines in Fig. 18 (a) and (b) are substantially shorter than those shown in Fig. 16 (a) and (b). The only parameter that differs in the simulations is the wind data. Thus, to examine the cause of this difference, Fig. 19 compares the simulated wind speeds and wind directions obtained from the WRF model with those obtained from the Fugui Cape buoy. Fig. 19 (a) compares the wind data from March 21 to 31, 2016, and Fig. 19 (b) compares the wind data for April, which is approximately the period of oil spill studied in the numerical simulation.

Fig. 19 (a) shows that the wind speeds from 09:00 AM on March 26 to 09:00 AM on March 27 obtained from the WRF model are much higher than those obtained from the Fugui Cape buoy. Table 2 shows the detailed values of observed and predicted wind speeds and wind directions in this period. These values reveal that the observed wind speeds range from 10.08 km/h (2.8 m/s) to 18.00 km/h (5 m/s), whereas the predicted speeds range from 16.52 km/h (4.59 m/s) to 27.14 km/h (7.54 m/s). The observed wind directions vary between 23° and 195°, and the simulated ones vary between 25° and 67°, indicating that the wind is northeasterly. Because the front edge of the oil-spilled area was very close to the coast (approximately 200 m; Fig. 16), a strong northeasterly wind rapidly advected the oil particles to the coast and drove them move westward along the coastline, as shown in Fig. 18 (a). As mentioned in Section 2.2, when the oil particles reach the land boundary, 80% of particles are stranded and only 20% of particles are able to leave the coast. However, under the predicted wind conditions the left 20% oil particles return to the coast. Consequently, most oil particles are stranded in a small region of the coastline.

Although the predicted wind speeds and directions during April are quite similar to the observed values; however, on the first day of the simulation, from 09:00 AM on March 26 to 09:00 AM on March 27, most of the 1000 released oil particles were stranded on the coast within a restricted area, as shown in Fig. 18 (a). Thereafter, only a small portion of the oil particles were free to move. Consequently, the fouled coastline at the end of April (Fig. 18 (b)) is very similar to that shown in Fig. 18 (a). The observed wind speeds ranged from 2.8 to 5.0 m/s, and the observed wind directions ranged from 23° to 195°. The winds with a wider direction range moved the oil particles to a wider portion of the coast. The surface current speeds, which varied between −1 and 1 m/s, as shown in Fig. 11, were of the same order of magnitude as the wind speeds. Therefore, the reciprocating currents contributed to the westward and eastward extension of the fouled coastline, as shown in Fig. 16 (a) and (b).

The aforementioned results demonstrate that both the wind and current data are crucial for an accurate prediction of the oil-spill trajectories. In the future, the applicability of the proposed strategy should be assessed for oil-spill events occurred on the open sea. In addition to the prediction of oil-spill trajectories, in-situ measurements of oil-slick thickness, oil sedimentation range, and chemical substances are critical for understanding the detailed oil-weathering processes and the environmental impact on the marine ecosystem. However, they are beyond the scope of this research.

6. Summary

In this study, we propose a two-step oil-spill forecasting system for predicting the trajectories of oil slicks. First, an X-band radar is established to detect oil slicks close to the oil-spill site and obtain the location and extent of oil spills. For this purpose, a procedure for detecting the oil-slick area from radar images is developed.

The information of the location and extent of oil spills can be used as the initial conditions for simulating the subsequent oil-spill trajectories. Furthermore, because the radar can also measure the ocean surface currents, this information when combined with available wind data can provide a fast assessment of the oil-slick trajectories. The results are useful for the execution of rescue missions and for rapid deployment of emergency equipment.

The simulated water surface elevations and ocean surface current obtained from the SCHISM were compared with the monitoring data to verify the accuracy of the hydrodynamic model incorporated in the SCHISM. The comparison reveals that both results agree closely with the monitoring data.

After obtaining the surface elevation and current from the SCHISM, the Lagrangian particle-tracking model incorporated in the SCHISM was used to simulate the trajectories of oil spills under various wind conditions, such as the observed wind speeds and directions from a nearby data buoy, or the wind fields predicted by the WRF model.

The oil spill caused by the container ship T. S. Taipei, which occurred during March 2016, was used as a case study for testing the capability of the proposed oil-tracking strategy, especially for events that happen very close to the coast.

When the wind data from the nearby Fugui Cape buoy were used, the simulated fouled coastline obtained from the SCHISM was very similar to that obtained from the field observation provided by the EPA, Taiwan. However, the contaminated coastline predicted using the wind data obtained from the WRF model was much shorter than the observed

one. The reasons for this difference were revealed after comparing the simulated and observed wind speeds and wind directions. Because the ship was stranded very close to the coast, the oil slicks moved to the coast within 1 day of the event.

In the future, the proposed strategy should be applied to oil-spill events occurring on the open sea to examine its suitability for wider applications.

Acknowledgments

The authors would like to thank Taiwan Ocean Research Institute for providing current data from the CODAR for verifying the accuracy of the simulated surface currents. Some simulations presented in this paper were conducted using the Sciclone cluster at the College of William and Mary, which was established under the auspices of the National Science Foundation, the Virginia Port Authority, Virginia's Commonwealth Technology Research Fund, and the Office of Naval Research. The authors are also grateful to the anonymous reviewers for their helpful comments and suggestions.

References

Alpers, W., Hühnerfuss, H., 1988. Radar signatures of oil films floating on the sea surface and the Marangoni effect. J. Geophys. Res. Oceans 93 (C4), 3642–3648.
Azevedo, A., Oliveira, A., Fortunato, A.B., Zhang, J., Baptista, A.M., 2014. A cross-scale numerical modeling system for management support of oil spill accidents. Mar. Pollut. Bull. 80, 132–147.
Beegle-Krause, C.J., 2001. General NOAA oil modeling environment (GNOME): a new spill trajectory model. In: IOSC 2001 Proceedings, Tampa, FL. vol. 2. pp. 865–871.
Beegle-Krause, C.J., 2018. Challenge and mysteries in oil spill fate and transport modeling. In: Oil Spill Environmental Forensics Case Studies; Chap. 9. Elsevier, pp. 187–199.
Chen, S.H., Dudhia, J., 2000. Annual Report: WRF Physics. Air Force Weather Agency, Boulder (38 pp.).
Chen, H.Z., Li, D.M., Li, X., 2007. Mathetical modeling of oil spill on the sea and application of the modeling in Daya Bay. J. Hydrodyn. Ser. B 19 (3), 282–291.
Cheng, Y., Li, X., Xu, Q., Garcia-Pineda, O., Andersen, O.B., Pichel, W.G., 2011. SAR observation and model tracking of an oil spill event in coastal waters. Mar. Pollut. Bull. 62 (2), 350–363.
Clift, R., Grace, J.R., Weber, M.E., 1978. Bubbles, Drops, and Particles. Academic, New York.
Crone, T.J., Tolstoy, M., 2010. Magnitude of the 2010 Gulf of Mexico oil leak. Science 330, 634.
Delvigne, G., Sweeney, C.E., 1988. Natural dispersion of oil. Oil Chem. Pollut. 4, 281–310.
Diop, S., Barusseau, J.P., Descamps, C. (Eds.), 2014. The Land/Ocean Interactions in the Coastal Zone of West and Central Africa. Springer.
EPA Taiwan, 2016. http://enews.epa.gov.tw/enews/fact_index.asp (in Chinese).
Fay, J.A., 1969. The spread of oil slicks on a calm sea. In: Hoult, D.P. (Ed.), Oil on the Sea. Ocean Technology, Springer, Boston, MA.
Fernando, H.J., 2012. Handbook of Environmental Fluid Dynamics, Volume Two: Systems, Pollution, Modeling, and Measurements. CRC press.
Fingas, M.F., 1996. The Evaporation of Crude Oil and Petroleum Products. PhD Dissertation. McGill University, Montreal, Canada, pp. 181.
Fingas, M.F., 2011. Oil Spill Science and Technology, Prevention, Response, and Cleanup. Elsevier, Boston, MA978-1-85617-943-0.
Fingas, M.F., 2014a. Handbook of Oil Spill Science and Technology. John Wiley & Sons.
Fingas, M.F., 2014b. Water-in-oil emulsions: formation and prediction. J. Pet. Sci. Res. 3 (1), 38–49.
Fingas, M.F., Brown, C.E., 1997. Review of oil spill remote sensing. Spill Sci. Technol. Bull. 4 (4), 199–208.
Fingas, M.F., Brown, C.E., 2014. Review of oil spill remote sensing. Mar. Pollut. Bull. 83 (1), 9–23.
Fingas, M.F., Fieldhouse, B., 2003. Studies of the formation of water-in-oil emulsions. Mar. Pollut. Bull. 47, 369–396.
Fingas, M.F., Fieldhouse, B., 2011. Studies on water-in-oil products from crude oils and petroleum products. Mar. Pollut. Bull. 64, 272–283.
Forget, P., Brochu, P., 1996. Slicks, waves and fronts observed in sea coastal area by an X-band airborne synthetic aperture radar. Remote Sens. Environ. 57, 1–12.
Fredj, E., Kohut, J., Roarty, H., Lu, J.W., 2017. Evaluation of the HF-Radar network system around Taiwan using normalized cumulative Lagrangian separation. In: EGU General Assembly Conference Abstracts. vol. 19. pp. 19137.
French-McCay, D.P., 2003. Development and application of damage assessment modeling: Example assessment for the North Cape oil spill. Mar. Pollut. Bull. 47, 341–359.
French-McCay, D.P., 2004. Oil spill impact modeling: development and validation. Environ. Toxicol. Chem. 23 (10), 2441–2456.
French-McCay, D.P., Jayko, K., Li, Z., Horn, M., Kim, Y., Isaji, T., Crowley, D., Spaulding, M., Decker, L., Turner, C., Zamorski, S., Fontenault, J., Shmookler, R., Rowe, J.J., 2015. Technical Reports for Deepwater Horizon Water Column Injury Assessment – WC_TR14: Modeling Oil Fate and Exposure Concentrations in the Deepwater Plume and Cone of rising Oil Resulting From the Deepwater Horizon Oil Spill. DWH NRDA Water Column Technical Working Group Report. Prepared for National Oceanic and Atmospheric Aministration by RPS ASA, South Kingstown, RI, USA (September 29, 2015. Administrative Record no. DWH-AR0285776.pdf).
Freudenburg, W.R., Gramling, R., 2011. Blowout in the Gulf – The BP Oil Spill Disaster and the Future of Energy in America, Chapter 9: Cleaning up. The MIT Press, Cambridge, Massachusetts.
Gangeskar, R., 2002. Ocean current estimated from X-band radar sea surface images. IEEE Trans. Geosci. Remote Sens. 40, 783–792.
Gundlach, E.R., Kana, T.W., Boehm, P.D., 1985. Modeling spilled oil partitioning in nearshore and surf zone areas. In: 1985 Int. Oil Spill Conf. pp. 379–383.
Guo, W.J., Wang, Y.X., 2009. A numerical oil spill model based on a hybrid method. Mar. Pollut. Bull. 58 (5), 726–734.
Haney, R.L., 1991. On the pressure gradient force over steep topography in sigma coordinate ocean models. J. Phys. Oceanogr. 21, 610–619.
Herbers, T.H.C., Jessen, P.F., Janssen, T.T., Colbert, D.B., MacMahan, J.H., 2012. Observing ocean surface waves with GPS-tracked buoys. J. Atmos. Ocean. Technol. 29, 944–959.
Hessner, K., Reichert, K., Borge, J., Stevens, C., Smith, M., 2014. High-resolution X-band radar measurements of currents, bathymetry and sea state in highly inhomogeneous coastal areas. Ocean Dyn. 64, 989–998.
Huang, J.C., 1983. A review of the state-of-the-art of oil spill fate/behavior models. In: Proc. 1983 Oil Spill Conf., San Antonio, TX, pp. 313–323.
Huang, N.E., Shen, Z., Long, S.R., Wu, M.C., Shih, E.H., Zheng, Q., Tung, C.C., Liu, H.H., 1998. The empirical mode decomposition method and the Hilbert spectrum for non-stationary time series analysis. Proc. Roy. Soc. London A 454, 903–995.
Huang, H.Y., Chang, C.M., Chang, C.H., 2016. Impact assessment of shoreline oiling caused by stranded ships – Case study of the container ship T.S. Taipei. In: 2016 Conference on Weather Analysis and Forecasting, A5–9, pp. 1–6. October 4–5, 2016. Central Weather Bureau, Taipei (in Chinese).
Kanevsky, M.B., 2008. Radar Imaging of the Ocean Waves. Elsevier Science.
Klemas, V., 2010. Tracking oil slicks and predicting their trajectories using remote sensors and models: case studies of the Sea Princess and Deepwater Horizon oil spills. J. Coast. Res. 26 (5), 789–797.
Kujawinski, E.B., Kido Soule, M.C., Valentine, D.L., Boysen, A.K., Longnecker, K., Redmond, M.C., 2011. Fate of dispersants associated with the Deepwater Horizon oil spill. Environ. Sci. Technol. 45, 1298–1306.
Lehr, W.J., Simecek-Beatty, D., 2000. The relations of Langmuir circulation processes to the standard oil spill spreading, dispersion, and transport algorithms. Spill Sci. Technol. Bull. 6, 247–253.
Lehr, W.J., Wesley, D., Simecek-Beatty, D., Jones, R., Kachook, G., Lankford, J., 2000. Algorithm and interface modifications of the NOAA oil spill behavior model. In: Proceedings of the 23rd Arctic and Marine Oilspill Program (AMOP) Technical Seminar. vol. 2. pp. 525–540.
Leifer, I., Lehr, W.J., Simecek-Beatty, D., Bradley, E., Clark, R., Dennison, P., Wozencraft, J., 2012. State of the art satellite and airborne marine oil spill remote sensing: application to the BP Deepwater Horizon oil spill. Remote Sens. Environ. 124, 185–209.
Lin, M.C., Kao, J.C., 2016. Marine environmental protection: an application of the nanometer photo catalyst method on decomposition of benzene. Mar. Pollut. Bull. 105, 139–142.
Lin, Y.P., Huang, C.J., Chen, S.H., Doong, D.J., Kao, C.C., 2017. Development of a GNSS buoy for monitoring water surface elevations in estuaries and coastal areas. Sensors 17, 172. https://doi.org/10.3390/s17010172.
Liu, P., Li, Y., Xu, J., Zhu, X., 2017. Adaptive enhancement of X-band marine radar imagery to detect oil spill segments. Sensors 17, 2349. https://doi.org/10.3390/s17102349.
Mackay, D., Paterson, S., Trudel, K., 1980. A Mathematical Model of Oil Spill Behavior. Department of Chemical and Applied Chemistry, University of Toroto, Canada, pp. 39.
Mackay, D., Shiu, W.Y., Hossain, K., Stiver, W., McCurdy, D., Peterson, S., 1982. Development and Calibration of an Oil Spill Behavior Model. Report No. CG-D-27-83. U.S. Coast Guard, Research and Development Center, Groton, Connecticut, pp. 83.
Mellor, G.L., Yamada, T., 1982. Development of a turbulence closure model for geophysical fluid problems. Rev. Geophys. 20, 851–875.
Montgomery, D.C., Runger, G.C., 2010. Applied Statistics and Probability for Engineers. John Wiley & Sons, New York.
NAS, 2003. Oil in the Sea III, Inputs, Fates, and Effects. National Research Council, National Academies Press, Washington, D.C.
Nieto Borge, J.C., Guedes Soares, C., 2000. Analysis of directional wave fields using X-band navigation radar. Coast. Eng. 40 (4), 375–391.
Nieto Borge, J.C., Rodriguez, G.R., Hessner, K., Gonzalez, P.I., 2004. Inversion of marine radar images for surface wave analysis. J. Atmos. Ocean. Technol. 21, 1291–1300.
North, E.W., Hood, R.R., Chao, S.Y., Sanford, L.P., 2006. Using a random displacement model to simulate turbulent particle motion in a baroclinic frontal zone: a new implementation scheme and model performance tests. J. Mar. Syst. 60, 365–380.
North, E.W., Adams, E.E., Schlag, Z., Sherwood, C.R., He, R., Hyun, K.H., Socolofsky, S.A., 2011. Simulating oil droplet dispersal from the Deepwater Horizon Spill with a Lagrangian approach. In: Liu, Y., MacFadyen, A., Ji, Z.-G., Weisberg, R.H. (Eds.), Monitoring and Modeling the Deepwater Horizon Oil Spill: A Record-Breaking Enterprise. Amer. Geophys. Union, Washington, DC, pp. 217–226.
Otsu, N., 1979. A threshold selection method from gray-level histograms. IEEE Trans. Syst. Man Cybern, vol. 9 (1), 62–66.
Peterson, C.H., Rice, S.D., Short, J.W., Esler, D., Bodkin, J.L., Ballachey, B.E., Irons, D.B., 2003. Long-term ecosytem response to the Exxon Valdez oil spill. Science 302, 2082–2086.

Plant, W.J., 1990. Bragg scattering of electromagnetic waves from the air/sea interface. In: Geernaert, G.L., Plant, W.L. (Eds.), Surface Waves and Fluxes, Vol. II-Remote Sensing. Springer, Netherlands, pp. 41–108.
Reed, M., Gundlach, E., 1989. A coastal zone oil spill model: development and sensitivity studies. Oil Chem. Pollut. 5, 411–449.
Reed, M., Johansen, Ø., Brandvik, P.J., Daling, P., Lewis, A., Fiocco, R., MacKay, D., Prentki, R., 1999. Oil spill modeling towards the close of the 20th century: overview of the state of the art. Spill Sci. Technol. Bull. 5 (1), 3–16.
Reed, M., Daling, P., Brakstad, O., Singsaas, I., Faksness, L., Hetland, B., Ekrol, N., 2000. Oscar: a multi-component 3-dimensional oil spill contingency and response model. In: Proceedings of the Arctic and Marine Oil Spill Program (AMOP) Technical Seminar, Vancouver, CA, pp. 663–680.
Rodi, W., 1984. Turbulence Models and their Applications in Hydraulics: A State of the Art Review. International Association for Hydraulics Research, Delft, The Netherlands.
SCHISM development teams, 2016. SCHISM v5.3.1 Manual (November 26, 2016). http://ccrm.vims.edu/schismweb/schismmanualv5.3.pdf.
Schloen, J., Stanev, E.V., Grashorn, S., 2017. Wave-current interactions in the southern North Sea: the impact on salinity. Ocean Model 111, 19–37.
Schwartz, C.S., Liu, Z., Huang, X.Y., Kuo, Y.H., Fong, C.T., 2013. Comparing limited-area 3DVAR and hybrid variational-ensemble data assimilation methods for typhoon track forecast: sensitivity to outer loops and vortex relocation. Mon. Weather Rev. 141, 4350–4372.
Senet, C.M., Seemann, J., Ziemer, F., 2001. The near-surface current velocity determined from image sequences of the sea surface. IEEE Trans. Geosci. Remote Sens. 39 (3), 492–505.
Simecek-Beatty, D., 2011. Oil spill trajectory forecasting uncertainty and emergency response. In: Oil Spill Science and Technology, Prevention, Response, and Cleanup; Chap. 11. Elsevier, pp. 275–299.
Simecek-Beatty, D., Lehr, W.J., 2007. Trajectory Modeling of Marine Oil Spills. In: Oil Spill Environmental Forensics: Fingerprinting and Source Identification; Chap. 13. Academic Press, pp. 405–418.
Spaulding, M.L., 2017. State of the art review and future directions in oil spill modeling. Mar. Pollut. Bull. 115, 7–19.
Spaulding, M.L., Howlett, E., Anderson, E., Jayko, K., 1992. OILMAP: a global approach to spill modeling. In: 15th Arctic and Marine Oil Spill Program. Technical Seminar, Edmonton, Alberta, Canada, June 9–11, 1992, pp. 15–21.
Stolzenbach, K.D., Madsen, O.S., Adams, E.E., Pollack, A.M., Cooper, C.K., 1977. A Review and Evaluation of Basic Techniques for Predicting the Behavior of Surface oil Slicks. Rep. 22, Department of Civil Engineering, Massachusetts Institute of Technology, Cambridge.
Tarr, M.A., Zito, P., Overton, E.B., Olson, G.M., Adhikari, P.L., Reddy, C.M., 2016. Weathering of oil spilled in the marine environment. Oceanography 29, 126–135.
Tennyson, E.J., 1988. Shipborne radar as an oil spill tracking tool. In: Proceedings of the 11th Arctic and marine Oil Spill Program, Technical Seminar, Vancouver, June 7–9, 1988, pp. 385–390.
Tkalich, P., 2006. A CFD solution of oil spill problems. Environ. Model. Softw. 21, 271–282.
Tomas, L.M., Rodrigues, M., Fortunato, A.B., Azevedo, A., Leitão, P.C., Oliveira, A., Rocha, A., Lopes, J.F., Dias, J.M., 2014. Salinity modelling accuracy of a coastal lagoon: a comparative river flow analysis of basin model vs. traditional approaches. J. Coast. Res. 70, 586–591.
Tsai, C.H., Doong, D.J., Chen, Y.C., Yen, C.W., Maa, M.J., 2016. Tidal stream characteristics on the coast of Cape Fuguei in Northwestern Taiwan for a potential power generation site. Int. J. Mar. Energy 13, 193–205.
Umlauf, L., Burchard, H., 2003. A generic length-scale equation for geophysical turbulence models. J. Mar. Res. 6, 235–265.
Visser, A.W., 1997. Using random walk models to simulate the vertical distribution of particles in a turbulent water column. Mar. Ecol. Prog. Ser. 158, 275–281.
Wadsworth, A., Looyen, W.J., Reuter, R., Petit, M., 1992. Aircraft experiments with visible and infrared sensors. Int. J. Remote Sens. 13 (6 & 7), 1175–1199.
Wang, Y.H., Jan, S., Wang, D.P., 2003. Transports and tidal current estimates in the Taiwan Strait from shipboard ADCP observations (1999–2001). Estuar. Coast. Shelf Sci. 57, 193–199.
Weijenborg, A.J., 2015. Validation of X-band Radar-derived Current Measurements at the Sand Engine: The Relation Between Spatial Scale of Wave Dispersion Analysis and Accuracy. PhD thesis. Delft University of Technology, Netherlands (73 pages).
Wilcox, D.C., 1998. Reassessment of scale determining equation for advance turbulence models. AIAA J. 26, 1299–1310.
Wu, Z., Huang, N.E., 2008. Ensemble empirical mode decomposition: a noise assisted data analysis method. In: Advances in Adaptive Data Analysis. Vol. 1(1). World Scientific Publishing Company, pp. 1–41.
Young, I.R., Rosenthal, W., Ziemer, F., 1985. A three-dimensional analysis of marine radar images for the determination of ocean wave directionality and surface currents. J. Geophys. Res. Oceans Atmos. 90, 1049–1059.
Yu, H.-C., Zhang, Y.J., Yu, J.C.S., Terng, C., Sun, W., Ye, F., Wang, H.V., Wang, Z., Huang, H., 2017. Simulating multi-scale oceanic processes around Taiwan on unstructured grids. Ocean Model 119, 72–93.
Zelenke, B., O'Connor, C., Barker, C., Beegle-Krause, C.J., Eclipse, L., 2012. General NOAA Operational Modeling Environment (GNOME) Technical Documentation. U.S. Dept. of Commerce, NOAA Technical Memorandum NOS OR&R 40. Emergency Response Division, NOAA, Seattle, WA (105 pp.).
Zeng, X., Zhao, M., Dickinson, R.E., 1998. Intercomparison of bulk aerodynamic algorithms for the computation of sea surface fluxes using TOGA COARE and TAO data. J. Clim. 11, 2618–2644.
Zhang, Y.J., Baptista, A.M., 2008. SELFE: a semi-implicit Eulerian–Lagrangian finite-element model for cross-scale ocean circulation. Ocean Model 21, 71–96.
Zhang, Y.J., Ateljevich, E., Yu, H.C., Wu, C.H., Yu, J.C.S., 2015. A new vertical coordinate system for a 3D unstructured-grid model. Ocean Model 85, 16–31.
Zhang, Y.J., Ye, F., Stanev, E.V., Grashorn, S., 2016. Seamless cross-scale modeling with SCHISM. Ocean Model 102, 64–81.
Zheng, L., Yapa, P.D., 2000. Buoyant velocity of spherical and nonspherical bubbles/droplets. J. Hydraul. Eng. 126 (11), 852–854.